

UNIVERSIDAD DE LOS ANDES

MONOGRAPH

Orbits of black holes in galactic triaxial potentials

Author:

Juan S. BARBOSA COY

Advisor:

Jaime FORERO, Ph.D.

Monograph presented for the degree of physicist

Departamento de Física
Facultad de Ciencias
Universidad de los Andes

Bogotá, Colombia
May 15, 2019

UNIVERSIDAD DE LOS ANDES

Abstract

Facultad de Ciencias
Departamento de Física
Facultad de Ciencias
Universidad de los Andes

Monograph

Orbits of black holes in galactic triaxial potentials

by Juan S. BARBOSA COY

Observations have confirmed that black hole mergers can emit gravitational waves. For such cases, conservation of momentum dictates that the merged system must move away from its initial position, producing what is known as a black hole kick. The black hole can be kicked with velocities up to 3000 km/s, depending on the mass ratio and spin alignment of the bodies. The behaviour of the kicked black hole depends on the gravitational potential provided by the stars, gas and dark matter of the host galaxy. In this work we used triaxial galactic potentials to follow the fate of such black holes. Our model takes into account the effects of dynamical friction and accretion. We will show how the settling times (the time it takes to go back at the potential minimum after the kick) depend on the stellar mass density and what is the influence of the potential triaxiality to induce stochasticity on the orbits. We finalize by commenting how these results can impact abundance estimates of active galactic nuclei across cosmic times.

UNIVERSIDAD DE LOS ANDES

Resumen

Facultad de Ciencias
Departamento de Física
Facultad de Ciencias
Universidad de los Andes

Monografía

Órbitas de agujeros negros en potenciales triaxiales de galaxias

por Juan S. BARBOSA COY

Las observaciones han confirmado que las fusiones de agujeros negros pueden emitir ondas gravitacionales. Para tales casos, la conservación del impulso dicta que el sistema fusionado debe alejarse de su posición inicial, produciendo lo que se conoce como una patada de agujero negro. El agujero negro puede experimentar un *kick* con velocidades de hasta 3000 km/s, dependiendo de la proporción de masa y la alineación de espines de los cuerpos. El comportamiento del agujero negro depende del potencial gravitatorio provisto por las estrellas, el gas y la materia oscura de la galaxia huésped. En este trabajo, utilizamos potenciales galácticos triaxiales para seguir el destino de estos agujeros negros. Nuestro modelo tiene en cuenta los efectos de la fricción dinámica y la acreción del agujero negro. Mostraremos cómo los tiempos de asentamiento (el tiempo que se tarda en volver al mínimo potencial) dependen de la densidad de masa estelar y de la influencia de la triaxialidad del potencial, la cual induce estocasticidad en las órbitas. Finalizamos comentando cómo estos resultados pueden impactar las estimaciones de abundancia de núcleos galácticos activos a través de los tiempos cósmicos.

Contents

Abstract	iii
Resumen	v
List of Figures	viii
List of Tables	xi
1 Introduction	1
2 Methodology	5
1 Densities profiles	6
1.1 Dark matter halo	6
1.2 Stellar density	7
1.3 Gas density	8
2 Equation of motion	8
2.1 Dynamical friction	8
2.2 Accretion onto the black hole	9
2.3 Initial conditions and numerical integration	10
3 Definitions	10
3.1 Return time	10
3.2 Return mass	10
4 Spherical setup	11
4.1 Virial radius	11
4.2 Dark matter halo	11
4.3 Stellar profile	11
4.4 Gas profile	12
5 Triaxial setup	12
3 Results and discussion	19
1 Spherical study	19
1.1 Effect of the baryonic fraction	20
1.2 Effect of the power law exponent	20

1.3	Effect of the stellar fraction	22
2	Triaxial study	25
2.1	Return distributions	27
2.2	Correlation between mass and time	29
2.3	Triaxial vs Spherical galaxies	29
4	Conclusions	33
A	Computational setup	35
1	Units	35
1.1	Universal gravitational constant	36
1.2	Hubble parameter	36
2	Critical density and Virial Radius	36
B	Time integration	39
C	Lyapunov exponents	43
D	Triaxial Galaxies	45
	References	61

List of Figures

1.1 Kick velocity distributions for different relative masses of the coalesced black holes. Random spin distributions are shown on the right side of the figure, while spins aligned with orbital momentum are shown on the right.	2
2.1 NGC4414 galaxy as seen by the Hubble telescope.	5
2.2 Dark matter concentration parameter as a function of the halo mass and the redshift.	7
2.3 Mass distributions for $R_{\text{vir}} = 0.69$ kpc (red line), $c = 4$, and $f_b = 0.156$	12
2.4 Dark matter densities comparison between spherical and triaxial cases.	13
2.5 Although the cumulative mass at the orange and blue dots is the same, the effective gravitational mass is different.	14
2.6 Error assessment of the numerical integrators, at $\vec{x} = (1, 0, 0)$ kpc.	16
2.7 Differences for analytical and numerical integration of the potentials gradients. .	17
3.1 Upper two plots show the output of a single simulation, while the lower one shows most the local properties per data point.	19
3.2 Effect of the baryonic fraction in the orbit of the black hole.	20
3.3 Properties of the power law exponent.	21
3.4 Return times of the black hole for different initial speeds and stellar fractions. .	22
3.5 Fits for the coefficients in Equation 3.5	23
3.6 Constructed surface of return times of the black hole for different initial speeds and stellar fractions.	24
3.7 Phase space generated with different stellar fractions, for an initial velocity $\vec{v} = 90\hat{i}$ kpc/Gyr.	24
3.8 Phase space generated with different stellar fractions, for an initial velocity $\vec{v} = 60\hat{i}$ kpc/Gyr.	25
3.9 Distributions of initial speeds for the triaxial lunches. θ describes the polar angle and ϕ the azimuth.	26
3.10 Distribution of the 30 pair of values for the y and z semiaxis.	26
3.11 Mass distributions of the returned black hole, for the 28 triaxial lunches (blue) and for an spherical galaxy.	27

3.12	Return time distributions, for the 30 triaxial lunches (blue) and for an spherical galaxy. Below, the cumulative probability of the purple curve.	28
3.13	Correlation between the return times and the return masses.	30
3.14	Probability distributions for the galaxies with higher and lower (red and blue) triaxial parameters, for the return properties as a function of the initial speed.	31
3.15	Relative distribution of the return properties as a function of the initial speed.	31
A.1	Floating point precision for different values, for a 32 bit and 64 bit holders.	35
A.2	Dependency of the Hubble parameter with redshift.	37
B.1	Leapfrog integration scheme	39
B.2	Energy variations of the Leapfrog scheme	40
C.1	Representation of three arbitrary close orbits, and their evolution in time.	43
C.2	Separation in time between orbits with initial distances of $\delta = 1 \times 10^{-4}$ kpc.	44
D.1	Distribution of the different properties for the galaxy with $a_1 = 1, a_2 = 1.0e + 00, a_3 = 4.6 \times 10^{-1}$	45
D.2	Distribution of the different properties for the galaxy with $a_1 = 1, a_2 = 9.3 \times 10^{-1}, a_3 = 2.6 \times 10^{-1}$	46
D.3	Distribution of the different properties for the galaxy with $a_1 = 1, a_2 = 9.6 \times 10^{-1}, a_3 = 7.0 \times 10^{-1}$	46
D.4	Distribution of the different properties for the galaxy with $a_1 = 1, a_2 = 8.7 \times 10^{-1}, a_3 = 1.3 \times 10^{-1}$	47
D.5	Distribution of the different properties for the galaxy with $a_1 = 1, a_2 = 6.9 \times 10^{-1}, a_3 = 1.2 \times 10^{-2}$	47
D.6	Distribution of the different properties for the galaxy with $a_1 = 1, a_2 = 6.8 \times 10^{-1}, a_3 = 2.2 \times 10^{-1}$	48
D.7	Distribution of the different properties for the galaxy with $a_1 = 1, a_2 = 6.3 \times 10^{-1}, a_3 = 2.8 \times 10^{-1}$	48
D.8	Distribution of the different properties for the galaxy with $a_1 = 1, a_2 = 5.7 \times 10^{-1}, a_3 = 3.3 \times 10^{-1}$	49
D.9	Distribution of the different properties for the galaxy with $a_1 = 1, a_2 = 4.8 \times 10^{-1}, a_3 = 3.1 \times 10^{-2}$	49
D.10	Distribution of the different properties for the galaxy with $a_1 = 1, a_2 = 6.4 \times 10^{-1}, a_3 = 4.8 \times 10^{-1}$	50
D.11	Distribution of the different properties for the galaxy with $a_1 = 1, a_2 = 5.0 \times 10^{-1}, a_3 = 1.7 \times 10^{-1}$	50
D.12	Distribution of the different properties for the galaxy with $a_1 = 1, a_2 = 5.8 \times 10^{-1}, a_3 = 4.1 \times 10^{-1}$	51

D.13 Distribution of the different properties for the galaxy with $a_1 = 1, a_2 = 7.5 \times 10^{-1}, a_3 = 6.8 \times 10^{-1}$	51
D.14 Distribution of the different properties for the galaxy with $a_1 = 1, a_2 = 4.2 \times 10^{-1}, a_3 = 7.4 \times 10^{-2}$	52
D.15 Distribution of the different properties for the galaxy with $a_1 = 1, a_2 = 6.4 \times 10^{-1}, a_3 = 5.5 \times 10^{-1}$	52
D.16 Distribution of the different properties for the galaxy with $a_1 = 1, a_2 = 4.8 \times 10^{-1}, a_3 = 2.9 \times 10^{-1}$	53
D.17 Distribution of the different properties for the galaxy with $a_1 = 1, a_2 = 3.9 \times 10^{-1}, a_3 = 5.2 \times 10^{-2}$	53
D.18 Distribution of the different properties for the galaxy with $a_1 = 1, a_2 = 7.5 \times 10^{-1}, a_3 = 7.1 \times 10^{-1}$	54
D.19 Distribution of the different properties for the galaxy with $a_1 = 1, a_2 = 3.7 \times 10^{-1}, a_3 = 2.8 \times 10^{-1}$	54
D.20 Distribution of the different properties for the galaxy with $a_1 = 1, a_2 = 2.8 \times 10^{-1}, a_3 = 1.5 \times 10^{-1}$	55
D.21 Distribution of the different properties for the galaxy with $a_1 = 1, a_2 = 3.2 \times 10^{-1}, a_3 = 2.4 \times 10^{-1}$	55
D.22 Distribution of the different properties for the galaxy with $a_1 = 1, a_2 = 2.7 \times 10^{-1}, a_3 = 2.0 \times 10^{-1}$	56
D.23 Distribution of the different properties for the galaxy with $a_1 = 1, a_2 = 4.8 \times 10^{-1}, a_3 = 4.6 \times 10^{-1}$	56
D.24 Distribution of the different properties for the galaxy with $a_1 = 1, a_2 = 4.8 \times 10^{-1}, a_3 = 4.6 \times 10^{-1}$	57
D.25 Distribution of the different properties for the galaxy with $a_1 = 1, a_2 = 3.5 \times 10^{-1}, a_3 = 3.3 \times 10^{-1}$	57
D.26 Distribution of the different properties for the galaxy with $a_1 = 1, a_2 = 1.1 \times 10^{-1}, a_3 = 5.3 \times 10^{-2}$	58
D.27 Distribution of the different properties for the galaxy with $a_1 = 1, a_2 = 2.0 \times 10^{-1}, a_3 = 1.9 \times 10^{-1}$	58
D.28 Distribution of the different properties for the galaxy with $a_1 = 1, a_2 = 6.6 \times 10^{-2}, a_3 = 6.1 \times 10^{-2}$	59

List of Tables

2.1	ψ values for the studied density profiles	14
2.2	$\nabla\Phi(\vec{x})$ values for the studied density profiles	15
2.3	Weighing functions and intervals of integration for Gauss quadratures	15
3.1	Parameters of the fitted gaussians in Figure 3.11.	27
3.2	Fitted values for the parameters in Equation 3.11, by using Figure 3.12.	29
A.1	Units of measure used on the simulations.	36
B.1	Φ values for the studied density profiles	40

Chapter 1

Introduction

The Theory of General Relativity by Albert Einstein was published in 1915, from which arise predictions such as gravitational waves, gravitational lenses, and time dilation. The term "gravitational waves" was introduced for the first time in a Henri Poincaré publication of 1905, in which he proposed the first equation for an invariant gravitational field before Lorentz transformations [1, 2]. At present, gravitational waves are understood as the periodic variations of the geometry of space-time, and have their origin in that the energy and moment density of a gravitational field act in turn as sources of gravity [3]. Although more than 100 years have passed since the publication of the theory, even today there are gaps in the understanding and implications of Einstein's equations. The foregoing is due, in part, to the difficulty of solving the equations for physical situations of interest. For example, gravitational waves can only be solved analytically for weak fields by using a linear form of these equations. However, at the experimental level it is only possible to detect gravitational waves from highly massive bodies, such as binary black hole systems, which only have strong fields. In 2016 a gravitational wave was detected for the first time in the history of mankind, and this discovery was recognized by the scientific community in 2017 with the Nobel Prize in Physics [4].

In particular for binary systems (two bodies orbiting around their center of mass), there is a phenomenon known as *recoil* or *kick*. This is because when considering General Relativity, the movement of bodies generates waves that carry momentum and energy, and that alters the trajectories previously predicted by the Theory of Universal Gravitation by Sir. Isaac Newton, where the solution to the equations of motion are elliptical trajectories in accordance with the laws of Kepler [3–5]. This causes that little by little the orbit decays and the two objects merge into a single body. At the moment the fusion takes place, the amplitude of the wave increases considerably. This implies that there will be a movement of the new body in the direction opposite to the propagation of the wave, given by the conservation of linear momentum. It is this movement that is known by the name of recoil or kick and was first described by Bonnor and Rotenberg in 1966 [5, 6].

The fusion of two black holes of a binary system gives rise to a new one, being this one of the mechanisms by which supermassive black holes are generated. This type of black hole has been found in almost all galaxies [7], and is characterized by having masses between $10^4 M_{\odot}$ to 10^{10}

$M_\odot(M_\odot$, solar masses), with such masses, it is possible for black holes to give rise to quasars. It has also been found that its mass correlates with properties of the galaxy among which are the speed of dispersion, luminosity and the mass of the galactic bulge. It has even been thought that these correlations show a co-evolution process of black holes and their galaxies. Among the effects of setbacks on black holes, it has been found that they limit the formation of black holes to masses less than $10^{10} M_\odot$ [7].

Simulations of merger kicks have shown that the speed at which the resulting black hole moves, strongly depend on the relative orientation of the spins of the colliding black holes [8]. **Baker et al.** developed a set of equations fitting their numerical results, in which the mass ratio of the black holes ($q \equiv m_2/m_1 \leq 1$), the spin vectors and the binary orbital angular momentum vector $\vec{d}_{1,2} = \vec{S}_{1,2}/m_{1,2}$ are taken into account. By using the set of equations of **Baker et al.**, **Tanaka and Haiman** worked in the distribution of kick velocities of black holes with different masses and relative spin orientations. Their results show that speeds up to 3000 km/s are possible, slightly lower than the previous limit of 4000 km/s from older numerical relativistic studies.

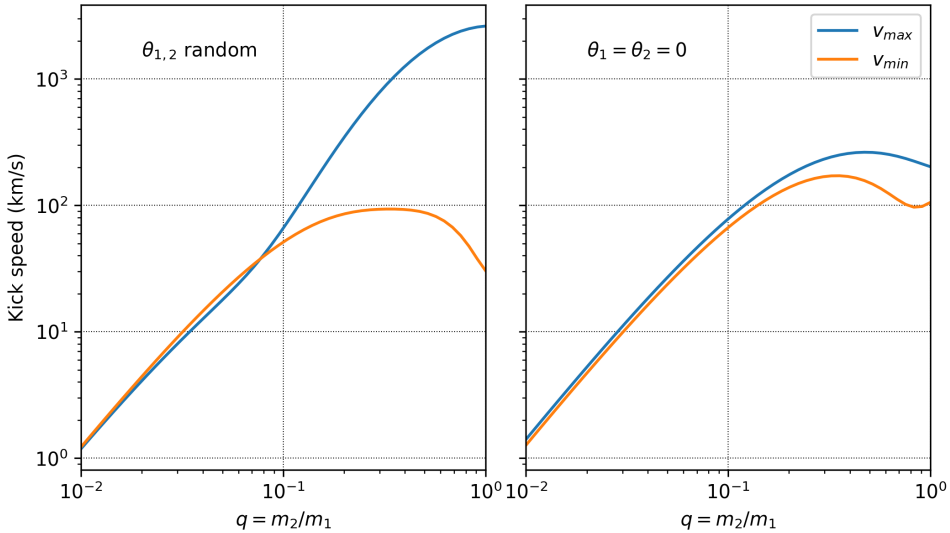


FIGURE 1.1: Kick velocity distributions for different relative masses of the coalesced black holes. Random spin distributions are shown on the right side of the figure, while spins aligned with orbital momentum are shown on the right.

When a black hole experiences a kick, the gravitational force, the dynamic friction, and the accretion act on it. The dynamic friction is due to the interaction of a body in movement with non-collisional matter such as dark matter and stars, which generates drag on it decreasing its speed. On the other hand, given the gravitational field of the black hole, small bodies that are in its path will be incorporated increasing the mass of the same, which causes a decrease in the

speed due to conservation of the momentum. Finally, the cosmological acceleration is due to the expansion of the universe and has a constant value for a given redshift (Z) [7].

Their effect on the black holes trajectory has been previously studied by Choksi et al., finding that variations in the value of the cosmological acceleration have little effect on the simulations [7]. For the accretion they determined that the increase of this factor lowers the time it takes for the black hole to return to its initial position, being this the most relevant effect for small-mass black holes. With respect to dynamic friction, they opted for a hybrid description between the models proposed by Ostriker and Escala et al., managing to take into account both the subsonic range and the highly supersonic range of the drag force [10, 11]. Finally, in their study they considered a spherically symmetric potential for the halo of the galaxy, bringing together the contributions of dark matter and visible matter in the same potential as mass distributions [7]. Nevertheless, all of these works consider only spherical/symmetrical potentials for the host galaxy of the black hole.

In this work we seek to analyze the effect of different triaxial potentials of the host galaxy, and initial velocities of the black hole in the return times and masses of the black hole to its galaxy. The above is of particular importance because with these potentials the angular momentum is not always conserved, the trajectories are not closed and the phase space is chaotic. The latter means that small variations in the initial conditions give rise to completely different final results. In addition, these potentials are observed in elliptical galaxies that rotate slowly [12, 13]. The chaotic component represents a challenge for the integration methods of the motion equation, since a numerical error is not different from a change in an initial condition. Because of this the Leapfrog method is choosed to integrate the orbits, and its conservation of energy is studied.

For this reason it is sought to perform each simulation using different numerical integrators, available in the Python and C library, REBOUND [14].

Chapter 2

Methodology

The host galaxy of the black hole is modeled as two mass distributions that are superimposed, one for dark matter and the other one for all the luminous or baryonic matter.

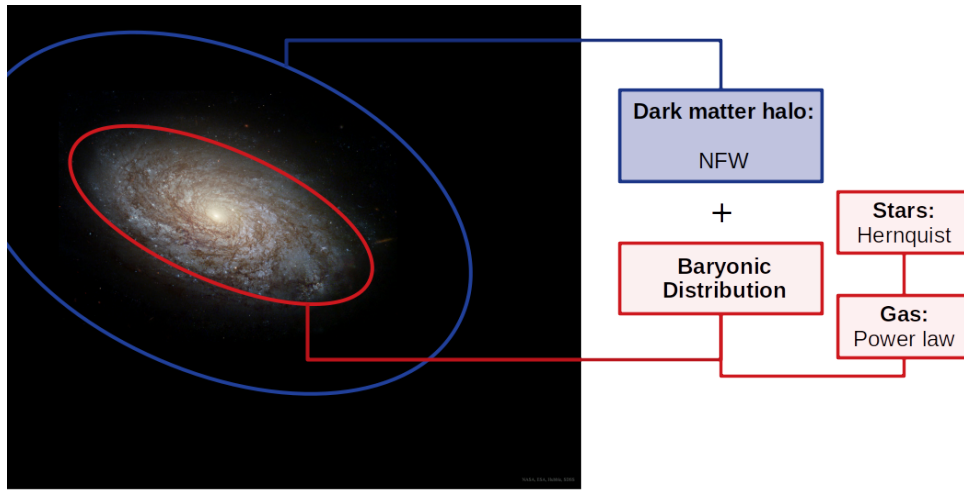


FIGURE 2.1: NGC4414 galaxy as seen by the Hubble telescope.

The dark matter halo used follows a NFW (Navarro–Frenk–White) profile, baryonic matter is divided in stars and gas. For the gas a power law profile with $r^{-2.2}$ is used, while for stars a Hernquist model is applied [7, 9]. The sum of all these components accounts for the total mass of the host (M_{total}), which remains constant through a simulation. The amount of baryonic matter is given by the baryonic fraction parameter (f_b), and the mass of stars by the stellar fraction parameter (f_s). Cumulative masses at the virial radius are defined as follows (Appendix A section 2):

$$M_{\text{DM}}(R_{\text{vir}}) = (1 - f_b)M_{\text{total}} \quad (2.1)$$

$$M_{\text{stars}}(R_{\text{vir}}) = f_s f_b M_{\text{total}} \quad (2.2)$$

$$M_{\text{gas}}(R_{\text{vir}}) = (1 - f_s)f_b M_{\text{total}} \quad (2.3)$$

Some of the simulation parameters are dependent of the cosmological model used, unless otherwise specified, all data is acquired using the Λ -CDM model with a matter density parameter $\Omega_M = 0.309$, $\Omega_\Lambda = 0.6911$, and a baryonic fraction $f_b = 0.156$ [7]. Also, as [Binney and Tremaine](#), argue, about 1 % of the stellar mass of galaxies, such as The Milky Way, are contained in the stellar halo, $f_s \equiv 0.01$, unless otherwise stated.

1 Densities profiles

1.1 Dark matter halo

For a dark matter halo following a NFW profile, the density at some distance r is given by the formula:

$$\rho_{\text{DM}}(r) = \frac{\rho_0^{\text{DM}}}{\frac{r}{R_s} \left(1 + \frac{r}{R_s}\right)^2} \quad (2.4)$$

Where R_s and ρ_0^{DM} are constants for a given dark matter halo. For a triaxial potential, it is said that density is constant within ellipsoids of ellipsoidal radius m . Using the Cartesian coordinates x_1, x_2, x_3 and a_1, a_2, a_3 the semi-axis of the ellipsoid, m is defined as follows:

$$m^2(\vec{x}) \equiv a_1^2 \left[\left(\frac{x_1}{a_1} \right)^2 + \left(\frac{x_2}{a_2} \right)^2 + \left(\frac{x_3}{a_3} \right)^2 \right] = x_1^2 + \left(\frac{a_1}{a_2} \right)^2 x_2^2 + \left(\frac{a_1}{a_3} \right)^2 x_3^2 \quad (2.5)$$

Considering a concentration parameter $c(M_{\text{total}}, z)$ of dark matter in the halo, the following relation holds for the viral radius R_{vir} and the scale radius R_s :

$$R_{\text{vir}} = c(M_{\text{total}}, z) R_s \quad (2.6)$$

Where the concentration parameter, dependence with the dark matter halo mass (M_{total}) and redshift is given by:

$$c(M_{\text{total}}, z) = c_0(z) \left(\frac{M_{\text{total}}}{10^{13} M_\theta} \right)^{\alpha(z)} \quad (2.7)$$

where $\alpha(z)$ and $c_0(z)$ were fitted using simulation data to the following functions [7]:

$$c_0(z) = \frac{4.58}{2} \left[\left(\frac{1+z}{2.24} \right)^{0.107} + \left(\frac{1+z}{2.24} \right)^{-1.29} \right] \quad (2.8)$$

$$\alpha(z) = -0.0965 \exp \left(-\frac{z}{4.06} \right) \quad (2.9)$$

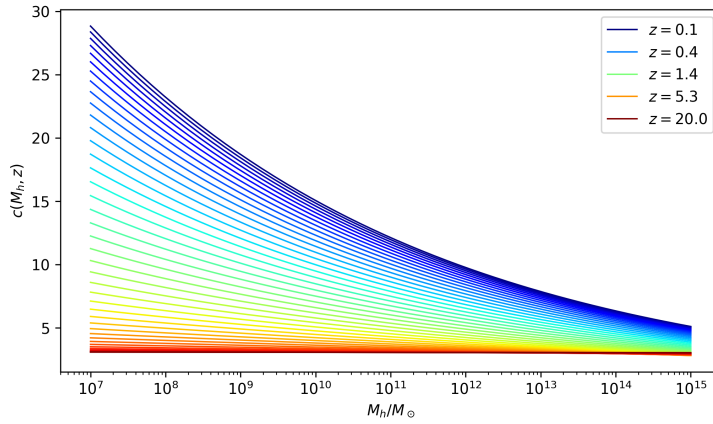


FIGURE 2.2: Dark matter concentration parameter as a function of the halo mass and the redshift.

For a fixed halo mass, as time passes (smaller redshift), concentration of dark matter will increase, as can be shown on Figure 2.2, nevertheless for high redshifts concentration is approximately constant at $c \approx 3$ for all halos [7]. Thus, the dark matter concentration parameter for all the simulations is fixed at this value.

1.2 Stellar density

Stellar density is modeled as a Hernquist profile with half-mass radius $R_{1/2} = 0.01R_{\text{vir}}$, as in Choksi et al. Density for a Hernquist profile is given by [16]:

$$\rho_s(r) = \frac{f_s f_b M_{\text{total}} \mathcal{R}_s}{2\pi r(r + \mathcal{R}_s)^3} \quad \mathcal{R}_s \text{ is known as scale length} \quad (2.10)$$

The half-mass radius, as the name implies, is the distance at which the cumulative mass is half the total mass [16]. By using the result in Equation 2.29:

$$R_{1/2} = (1 + \sqrt{2}) \mathcal{R}_s = 0.01 \left(\frac{M_{\text{total}} G}{100 H(t)^2} \right)^{1/3} \quad (2.11)$$

From which the scale length can be set as a function of the time when the kick occurs, and the mass of the host, as:

$$\mathcal{R}_s = \frac{0.01}{(1 + \sqrt{2})} \left(\frac{M_{\text{total}} G}{100 H(t)^2} \right)^{1/3} \approx 6.835 \times 10^{-4} \left(\frac{M_{\text{total}}}{H(t)^2} \right)^{1/3} \quad (2.12)$$

1.3 Gas density

For high redshift the baryonic profile resembles that of a gaseous galaxy, Choksi et al. use a constant density gas core of $r_0 = 1$ pc, followed by a power law of $r^{-n} = r^{-2.2}$. Density is described as follows: for $r \gg r_0$, $\rho_{\text{gas}}(r) \propto r^{-n}$ while for $r \ll r_0$, $\rho_{\text{gas}}(r) \approx \rho_0^{\text{gas}}$.

$$\rho_{\text{gas}}(r) = \frac{\rho_0^{\text{gas}}}{\left(1 + \frac{r}{r_0}\right)^n} \quad (2.13)$$

2 Equation of motion

Trajectories of the kicked black holes are obtained by numerically solving the equation of motion on Equation 2.14, where the first term on the right side of the equation is acceleration due to gravity, the second accounts for the drag of dynamical friction, while the third is the deceleration due to mass accretion of the black hole [7, 9].

$$\ddot{\vec{x}}(\vec{x}, \dot{\vec{x}}) = a_{\text{grav}}(\vec{x})\hat{x} + \left(a_{\text{DF}}(\vec{x}, \dot{\vec{x}}) - \dot{\vec{x}} \frac{\dot{M}_\bullet(x, \dot{x})}{M_\bullet}\right)\hat{x} \quad \text{where } M_\bullet \text{ is the black hole mass} \quad (2.14)$$

2.1 Dynamical friction

As the black hole travels through the galaxy, dark matter, stars and gaseous materials from the medium interact with the black hole adding a drag force due to friction. Drag force is different in nature depending on its source, collisionless components, such as dark matter and stars, apply a drag force to the black hole that follows the standard Chandrasekhar formula [7, 9, 15, 17].

$$a_{\text{DF}}^{\text{cl}}(\vec{x}, \dot{\vec{x}}) = -\frac{4\pi G^2}{\dot{x}^2} M_\bullet \rho(\vec{x}) \ln \Lambda \left(\text{erf}(X) - \frac{2}{\sqrt{\pi}} X e^{-X^2} \right), \quad \rho(\vec{x}) = \rho_{\text{DM}}(\vec{x}) + \rho_{\text{stars}}(\vec{x}) \quad (2.15)$$

$$X \equiv \frac{|\dot{x}|}{\sqrt{2}\sigma_{\text{DM}}} \quad \text{with } \sigma_{\text{DM}} = \sqrt{\frac{GM_{\text{DM}}}{2R_{\text{vir}}}} \quad (2.16)$$

σ_{DM} is called the local velocity dispersion of the dark matter halo, and since varies little over the entire host, can be taken as constant [7, 9]. The Coulomb logarithm ($\ln \Lambda$) is not known but authors take it in the range of 2 - 4 [7]. Gas on the other hand is collisional, special care must be taken since gas can cool behind a passing object, such as a black hole [7]. A hybrid model for the drag force was proposed by Tanaka and Haiman, in which both subsonic and supersonic velocities are possible. To do so, a mach number was defined as:

$$\mathcal{M}(\dot{x}) \equiv \frac{|\dot{x}|}{c_s} \quad (2.17)$$

where c_s is the local sound speed, which depends on local temperature. It was found that temperature inside the halo varies less than a factor of 3, thus on the simulation it is assumed that the entire halo is isothermal at the virial temperature (T_{vir}) [7]. The isothermal sound speed is [18]:

$$c_s = \sqrt{\frac{\gamma R}{M_w} T_{\text{vir}}} = \sqrt{\frac{\gamma R}{M_w} \left(\frac{\mu m_p G M_{\text{total}}}{2k_B R_{\text{vir}}} \right)} = \sqrt{\frac{\gamma R \mu m_p G}{2M_w k_B}} \sqrt{\frac{M_{\text{total}}}{R_{\text{vir}}}} \approx 0.614 \sqrt{\frac{M_{\text{total}}}{R_{\text{vir}}}} \text{ kpcGyr}^{-1} \quad (2.18)$$

where μ is the value of the mean molecular weight of the gas (M_w), m_p is the proton mass and γ is the adiabatic index [18]. Approximating the gas to a monoatomic one $\gamma \approx 5/3$, yields the last expression on [Equation 2.18](#). By knowing M , the acceleration caused by gas can be written as [7, 9]:

$$a_{\text{DF}}^{\text{C}}(\vec{x}, \dot{\vec{x}}) = -\frac{4\pi G^2}{\dot{x}^2} M_{\bullet} \rho_{\text{gas}}(\vec{x}) f(M) \quad (2.19)$$

with

$$f(M) = \begin{cases} 0.5 \ln \Lambda \left[\text{erf} \left(\frac{M}{\sqrt{2}} \right) - \sqrt{\frac{2}{\pi}} M e^{-M^2/2} \right] & \text{if } M \leq 0.8 \\ 1.5 \ln \Lambda \left[\text{erf} \left(\frac{M}{\sqrt{2}} \right) - \sqrt{\frac{2}{\pi}} M e^{-M^2/2} \right] & \text{if } 0.8 < M \leq M_{eq} \\ 0.5 \ln (1 - M^{-2}) + \ln \Lambda & \text{if } M > M_{eq} \end{cases} \quad (2.20)$$

M_{eq} is the mach number that fulfills the following equation:

$$\ln \Lambda \left[1.5 \left(\text{erf} \left(\frac{M}{\sqrt{2}} \right) - \sqrt{\frac{2}{\pi}} M e^{-M^2/2} \right) - 1 \right] - 0.5 \ln (1 - M^{-2}) = 0 \quad (2.21)$$

Numerically solving [Equation 2.21](#), yields $M_{eq} \approx 1.731$ for a value of the Coulomb logarithm $\ln \Lambda = 2.3$. The full acceleration due to dynamical friction is given by the sum of the noncollisional drag on [Equation 2.15](#) and [Equation 2.19](#):

$$a_{\text{DF}}(\vec{x}, \dot{\vec{x}}) = a_{\text{DF}}^{\text{cl}}(\vec{x}, \dot{\vec{x}}) + a_{\text{DF}}^{\text{C}}(\vec{x}, \dot{\vec{x}}) \quad (2.22)$$

2.2 Accretion onto the black hole

As the black hole accretes matter from the surroundings, an acceleration appears, due to the second law of Newton:

$$\vec{F} = \frac{d\vec{P}}{dt} = \dot{\vec{x}} \dot{M}_{\bullet} + M_{\bullet} \ddot{\vec{x}} \quad (2.23)$$

By considering conservation of momentum:

$$\ddot{\vec{x}} = -\dot{\vec{x}} \frac{\dot{M}_\bullet}{M_\bullet} \quad (2.24)$$

Two schemes describe the speed at which the black hole gains mass, on the first one the black hole undergoes Bondi-Hoyle-Littleton accretion [7, 9]:

$$\dot{M}_\bullet^{\text{BHL}}(\vec{x}, \dot{\vec{x}}) = \frac{4\pi G^2 \rho_G(\vec{x}) M_\bullet^2}{(c_s^2 + \dot{x}^2)^{3/2}} \quad \text{with } \rho_B(\vec{x}) = \rho_{\text{stars}}(\vec{x}) + \rho_{\text{gas}}(\vec{x}) \quad (2.25)$$

But, there is a limit of accretion for the black hole given by the Eddington luminosity:

$$\dot{M}_\bullet^{\text{Edd}} = \frac{(1-\epsilon)M_\bullet}{\epsilon t_{\text{Edd}}} \quad \epsilon = 0.1, \quad t_{\text{Edd}} = 0.44 \text{ Gyr} \quad (2.26)$$

Thus, the final accretion rate is given by:

$$\dot{M}_\bullet(\vec{x}, \dot{\vec{x}}) = \begin{cases} \dot{M}_\bullet^{\text{BHL}}(\vec{x}, \dot{\vec{x}}) & \text{if } \dot{M}_\bullet^{\text{BHL}} < \dot{M}_\bullet^{\text{Edd}} \\ \dot{M}_\bullet^{\text{Edd}} & \text{else} \end{cases} \quad (2.27)$$

2.3 Initial conditions and numerical integration

For all simulations the virial radius remains constant through the simulation. The virial radius is fixed at the start of every simulation depending on the redshift at which the kick occurs, the chosen densities profiles and the mass of the host galaxy. Sound speed also remains constant for a simulation, as it depends on R_{vir} and the mass of the host. Cosmological acceleration is ignored at all times as in [Tanaka and Haiman](#), as it has been found that it only marginally affects black hole orbits [7]. The initial position of the black hole is always $\vec{x} = (1, 1, 1)$ pc.

Numerical integration is carried out using a Leapfrog scheme on REBOUND with the C programming language [14], with time steps of a thousand years, the simulations are stopped when the system destabilizes and starts gaining energy, due to singularities at $x \rightarrow 0$ and $\dot{x} \rightarrow 0$, or if they simply last more than the current age of the universe.

3 Definitions

3.1 Return time

Time required by the black holes orbit to have a maximum distance of less than $0.01R_{\text{vir}}$.

3.2 Return mass

Mass at the return time of the black hole.

4 Spherical setup

4.1 Virial radius

Since all of the density profiles are spherically symmetrical, it follows from [Equation A.4](#) that:

$$\frac{M_{\text{total}}}{4/3\pi R_{\text{vir}}^3} = 75 \frac{H(t)^2}{\pi G} \quad (2.28)$$

$$R_{\text{vir}} = \left(\frac{M_{\text{total}} G}{100 H(t)^2} \right)^{1/3} \quad (2.29)$$

4.2 Dark matter halo

For a dark matter halo following a NFW profile, the cumulative mass $M_{\text{DM}}(r)$ within some radius r is given by the integral of the density over a volume. Since [Equation 2.4](#) is spherically symmetrical, the only dependance of the integral is with distance. On [Equation 2.30](#) the r'^2 comes from the Jacobian of spherical coordinates, and the 4π from the solid angle.

$$M_{\text{DM}}(r) = \int_0^r 4\pi r'^2 \rho_{\text{DM}}(r') dr' = 4\pi \rho_0^{\text{DM}} R_s^3 \left[\ln \left(\frac{R_s + r}{R_s} \right) - \frac{r}{R_s + r} \right] \quad (2.30)$$

By using [Equation 2.6](#) one can obtain the value of ρ_0^{DM} by evaluating [Equation 2.30](#) at R_{vir} .

$$M_{\text{DM}}(R_{\text{vir}}) = 4\pi \rho_0^{\text{DM}} R_s^3 \left[\ln \left(\frac{R_s + c(M_{\text{total}}, z) R_s}{R_s} \right) - \frac{c(M_{\text{total}}, z) R_s}{R_s + c(M_{\text{total}}, z) R_s} \right] = (1 - f_b) M_{\text{total}} \quad (2.31)$$

$$\rho_0^{\text{DM}} = \frac{(1 - f_b) M_{\text{total}}}{4\pi \left(\frac{R_{\text{vir}}}{c(M_{\text{total}}, z)} \right)^3 \left[\ln(1 + c(M_{\text{total}}, z)) - \frac{c(M_{\text{total}}, z)}{1 + c(M_{\text{total}}, z)} \right]} \quad (2.32)$$

4.3 Stellar profile

Integrating [Equation 2.10](#) from 0 to r yields:

$$M_s(r) = \frac{f_s f_b M_{\text{total}} r^2}{(r + \mathcal{R}_s)^2} \quad (2.33)$$

4.4 Gas profile

The cumulative mass is found by integrating [Equation 2.13](#) in spherical coordinates.

$$\begin{aligned} M_{\text{gas}}(r) &= 4\pi\rho_0^{\text{gas}} r_0^3 \int_0^u \frac{u'^2}{(1+u')^n} du' \\ &= 4\pi\rho_0^{\text{gas}} r_0^3 (u+1)^{-n} \frac{-(u+1)(nu)^2 + 2[(u+1)^n - u^3 - 1] + nu[3u^2 + u - 2]}{(n-3)(n-2)(n-1)} \end{aligned}$$

where $u = r/r_0$, for $u \leq 0$ and $n \neq 1, 2, 3$

(2.34)

The value of the constant ρ_0^{gas} is found using a similar process as in [Equation 2.31](#) and [2.32](#).

$$\rho_0^{\text{gas}} = \frac{(1-f_s)f_b M_{\text{total}}}{(M_{\text{gas}}(R_{\text{vir}})/\rho_0^{\text{gas}})}$$
(2.35)

All of the profiles are shown on [Figure 2.3](#), where the effect of the stellar fraction can be seen.

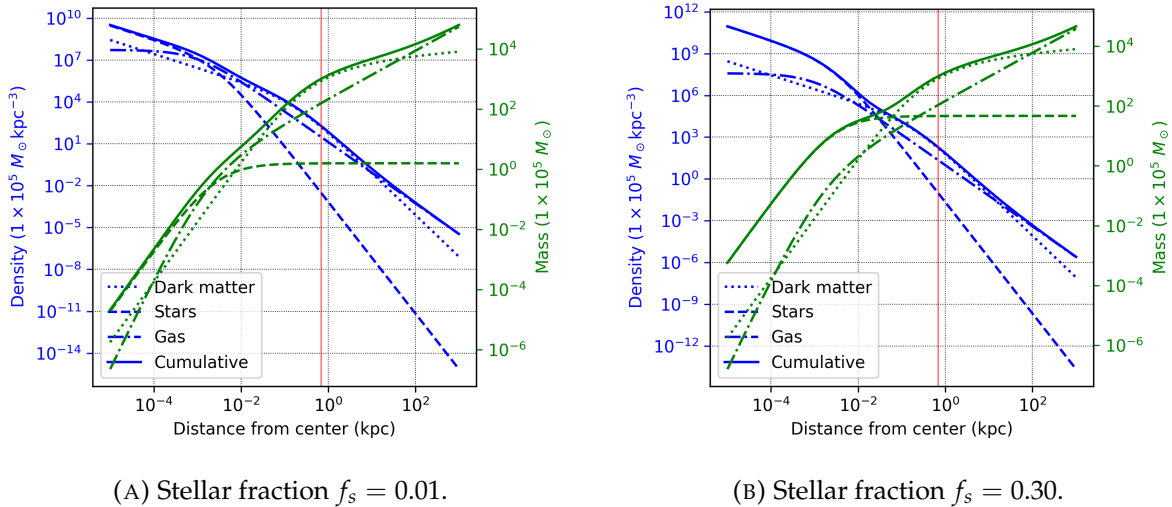


FIGURE 2.3: Mass distributions for $R_{\text{vir}} = 0.69$ kpc (red line), $c = 4$, and $f_b = 0.156$.

5 Triaxial setup

The host galaxy is modeled as a dark matter halo, stars and gas, just as the spherical case. Much of the profiles for each of the components remains the same, the only difference is that a thin shell of uniform density will have the geometry of an ellipsoid, and not that of a sphere. This is achieved by defining an ellipsoid radius m , that can be replaced for the spherical radius r , on equations [2.4](#), [2.10](#) and [Equation 2.13](#), as can be seen on [Figure 2.4](#).

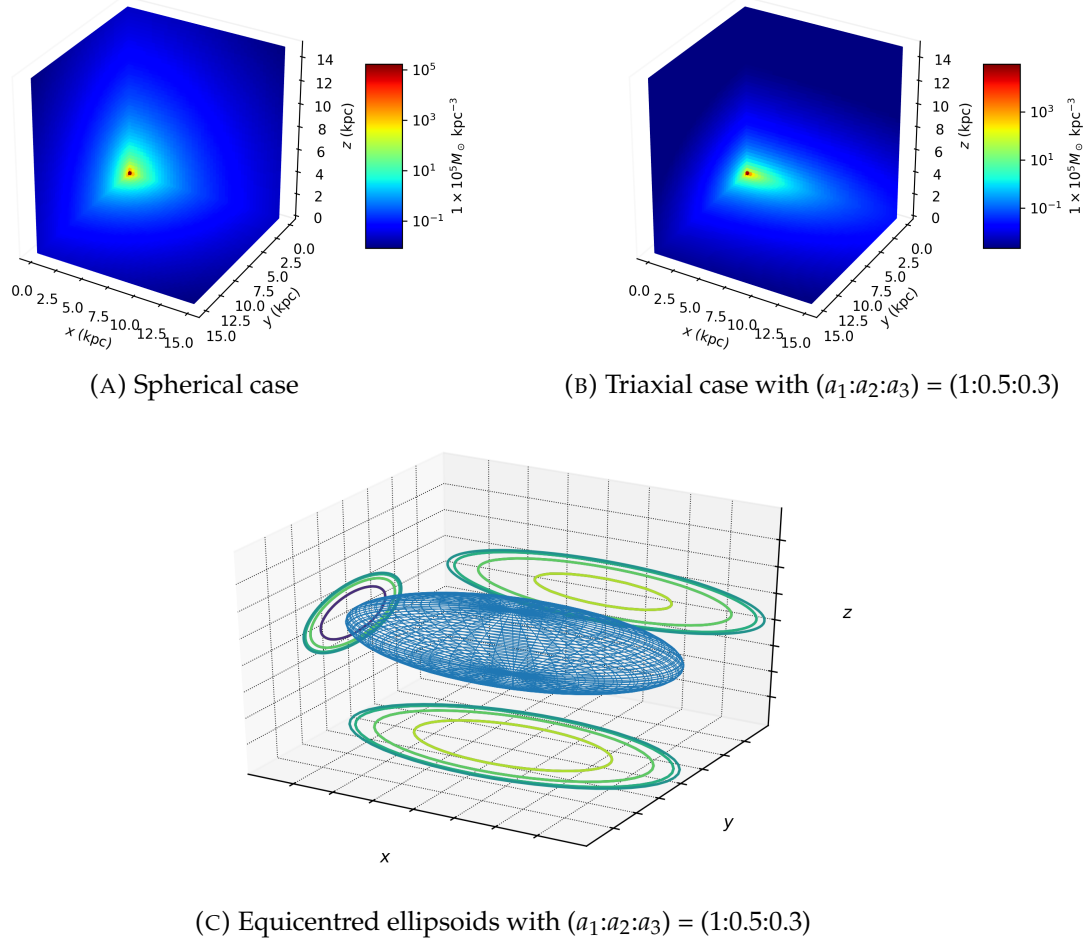


FIGURE 2.4: Dark matter densities comparison between spherical and triaxial cases.

A thin shell, whose inner and outer skins are the surfaces m and $m + \delta m$ is described by Equation 2.36, where $\tau \geq 0$ labels the surfaces [15].

$$m^2(\vec{x}, \tau) = a_1^2 \left(\frac{x_1^2}{\tau + a_1^2} + \frac{x_2^2}{\tau + a_2^2} + \frac{x_3^2}{\tau + a_3^2} \right) \quad (2.36)$$

Densities are used for the calculation of the dynamical friction and accretion onto the black hole. Although one might think that by integrating the density over an elliptical volume, the acceleration due to gravity would be given by $a_{\text{grav}} = GM(m)/m^2$, the later is not true because two points (x_1, x_2, x_3) and (x'_1, x'_2, x'_3) might have the same cumulative mass at m (black line), but the effective gravitational mass acting at each point is completely different (blue and orange lines) as it is shown in Figure 2.5.

Because of this, the potential due to a given triaxial density must be found. Calculating the gravitational potential for such configuration, challenged some great minds of the XVIII and

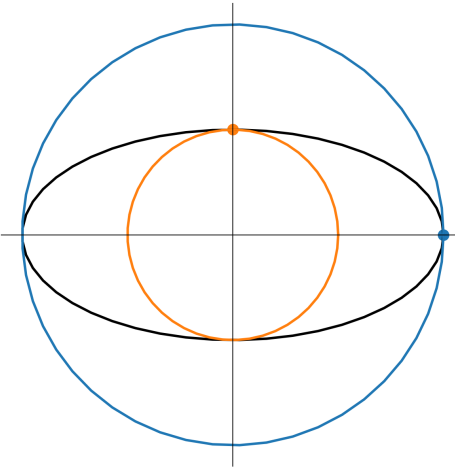


FIGURE 2.5: Although the cumulative mass at the orange and blue dots is the same, the effective gravitational mass is different.

XIX centuries [15]. To do so, the contributions of all ellipsoidal shells that make up the profile are taken into account, following Binney and Tremaine:

$$\psi(m) \equiv \int_0^{m^2} \rho(m'^2) dm'^2 = \int_0^m 2m' \rho(m') dm' \quad (2.37)$$

The potential of any body in which $\rho = \rho(m^2)$ is [15]:

$$\Phi(\vec{x}) = -\pi G \frac{a_2 a_3}{a_1} \int_0^\infty \frac{\psi(\infty) - \psi(m)}{\sqrt{(\tau + a_1^2)(\tau + a_2^2)(\tau + a_3^2)}} d\tau \quad m = m(\vec{x}, \tau) \quad (2.38)$$

TABLE 2.1: ψ values for the studied density profiles

Profile	$\psi(\infty) - \psi(m)$
NFW	$\frac{2R_s^3 \rho_0^{\text{DM}}}{R_s + m(\vec{x}, \tau)}$
Hernquist	$\frac{M_s \mathcal{R}_s}{2\pi (\mathcal{R}_s + m(\vec{x}, \tau))^2}$
Power-law	$\frac{2\rho_0^{\text{gas}} \left(\frac{m(\vec{x}, \tau) + r_0}{r_0} \right)^{-n} (m(\vec{x}, \tau) + r_0) (m(\vec{x}, \tau) (n-1) + r_0)}{(n-2) (n-1)}$

Most of the triaxials potentials cannot be analytically integrated, nevertheless it can be done numerically. Since the gravitational acceleration is given by the gradient of the potential, to numerically calculate the gradient, a total of 6 numerical integrals must be done (two for each

dimension, and then numerically differentiate). Another option is to take advantage of the fact that \vec{x} and τ are independent variables, thus:

$$\nabla \int f(\vec{x}, \tau) d\tau = \int [\nabla f(\vec{x}, \tau)] d\tau \quad (2.39)$$

By doing this, the number of numerical integrals reduces to 3. Defining a vector $\vec{\phi}$, whose components are given by:

$$\phi_i(x_i, \tau) = \frac{x_i}{(\tau + a_i^2)^{\frac{3}{2}} \prod_{i \neq j}^3 \sqrt{\tau + a_j^2}}, \quad \vec{\phi}(\vec{x}, \tau) = (\phi_1(x_1, \tau), \phi_2(x_2, \tau), \phi_3(x_3, \tau)) \quad (2.40)$$

Potentials for each of the components of the galaxy are found by calculating $\psi(\infty) - \psi(m)$ and replacing on [Equation 2.38](#).

TABLE 2.2: $\nabla\Phi(\vec{x})$ values for the studied density profiles

Profile	$\nabla\Phi(\vec{x})$
NFW	$2\pi G R_s^3 \rho_0 a_1 a_2 a_3 \int_0^\infty \frac{\vec{\phi}(\vec{x}, \tau) d\tau}{m(\vec{x}, \tau) (R_s + m(\vec{x}, \tau))^2}$
Hernquist	$G M_s \mathcal{R}_s a_1 a_2 a_3 \int_0^\infty \frac{\vec{\phi}(\vec{x}, \tau) d\tau}{m(\vec{x}, \tau) (\mathcal{R}_s + m(\vec{x}, \tau))^3}$
Power-law	$2\pi G a_1 a_2 a_3 \rho_0^{\text{gas}} \int_0^\infty \vec{\phi}(\vec{x}, \tau) \left(\frac{r_0}{m(\vec{x}, \tau) + r_0} \right)^n d\tau$

Two Gaussian quadrature integration schemes are tested, Gauss-Legendre and Gauss-Laguerre. Both schemes rely on the use of orthogonal polynomials whose roots yield the nodes x_i at which a function is evaluated, multiplied by a weighting value w_i in order to calculate its integral as in [Equation 2.41](#), where k is the degree of the polynomial used.

$$\int_a^b w(x) f(x) dx \approx \sum_{i=1}^k w_i f(x_i), \quad \text{where } w(x) \text{ is a weighting function} \quad (2.41)$$

TABLE 2.3: Weighing functions and intervals of integration for Gauss quadratures

Interval	Weighting function	Orthogonal polynomials
$[-1, 1]$	1	Legendre
$[0, \infty)$	e^{-x}	Laguerre

To make the integral proper, for the Gauss-Legendre quadrature, the following change of variable is done:

$$\omega = \frac{\tau^\gamma}{\tau^\gamma + 1}, \quad \tau = \left(\frac{\omega}{1 - \omega} \right)^{\frac{1}{\gamma}}, \quad d\tau = \frac{(-\frac{\omega}{\omega-1})^{\frac{1}{\gamma}}}{\gamma\omega(-\omega+1)} d\omega, \quad \gamma > 0 \quad (2.42)$$

By using Equation 2.42, the new interval is $[0, 1]$, thus, to use the Gauss-Legendre, the following change is done:

$$\int_0^1 f(x) dx = \frac{1}{2} \int_{-1}^1 f\left(\frac{x+1}{2}\right) dx \approx \frac{1}{2} \sum_{i=1}^k w_i f\left(\frac{x+1}{2}\right) \quad (2.43)$$

In the case of Gauss-Laguerre a weighting function is required, since none of the integrals on Table 2.2 has a term of the form $e^{-\tau}$, it is introduced by multiplying and dividing all expressions by e^τ .

$$\int_0^\infty e^{-x} e^x f(x) dx = \int_0^\infty e^{-x} g(x) dx = \sum_{i=1}^k w_i g(x), \quad \text{where } g(x) = e^x f(x) \quad (2.44)$$

To test the precision of the numerical approximation, integrals on Table 2.2 are compared with the potential generated by the spherical analog in which $\nabla\Phi = GM(r)/r^2$ by making all semi-axis equal to 1.

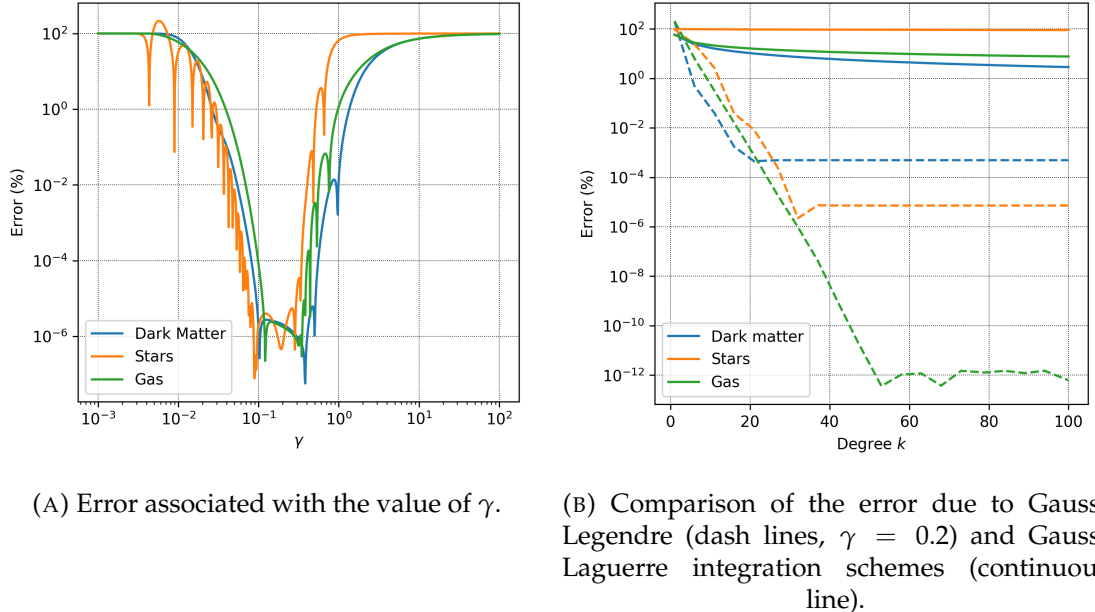


FIGURE 2.6: Error assessment of the numerical integrators, at $\vec{x} = (1, 0, 0)$ kpc.

Since γ is a free parameter in the Gauss-Legendre scheme, it must be optimized, results on Figure 2.6a show a stability region for all potentials close to $\gamma = 0.2$. On Figure 2.6b, a

comparison of the error for both Gauss schemes is made, finding that Gauss-Legendre is better for all potentials when the degree of the polynomial used is bigger than 10, and that after $k \approx 50$ there is no variation on the error with Gauss-Legendre.

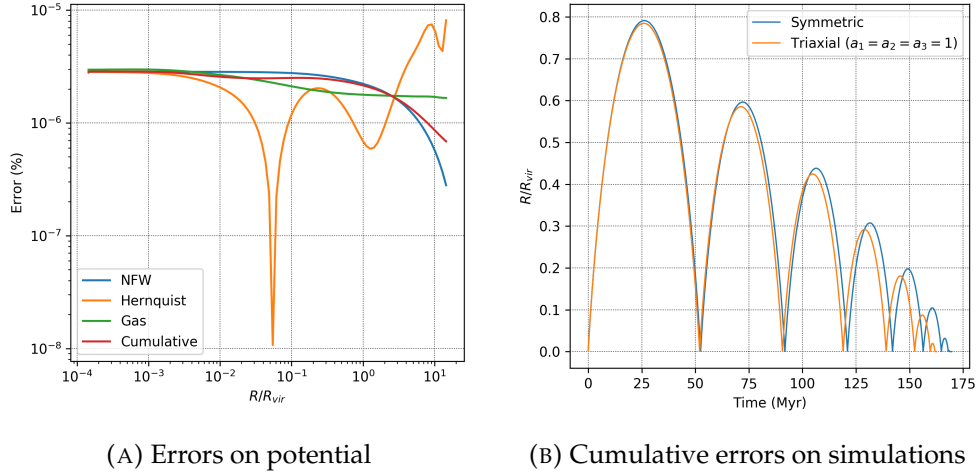


FIGURE 2.7: Differences for analytical and numerical integration of the potentials gradients.

Furthermore, error is not constant with distance, as can be seen on Figure 2.7a. In particular, the numerical error in the calculation of the gradient of the potential is associated to the gas, causing the orbits to change slightly due to cumulative errors in each time step.

Chapter 3

Results and discussion

1 Spherical study

For a single simulation, the following data is saved: iteration time, current position, speed, and the black hole mass. With these information, accelerations and densities can be later reconstructed as on [Figure 3.1](#).

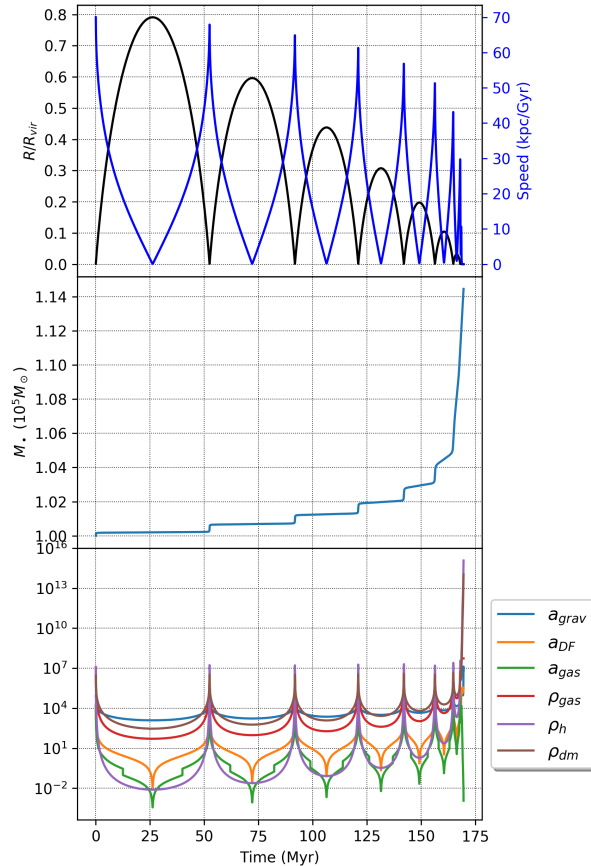


FIGURE 3.1: Upper two plots show the output of a single simulation, while the lower one shows most the local properties per data point.

1.1 Effect of the baryonic fraction

The cosmological model used has two main effects in the simulations. The virial radius depends in the value of the Hubble parameter, that changes for different red-shifts and cosmological models (Figure A.2), and the amount of matter in the universe. The effect of the later can be seen on Figure 3.2, where results for a galaxy made by dark matter only allow the black hole to get further away, and dissipate energy slower.

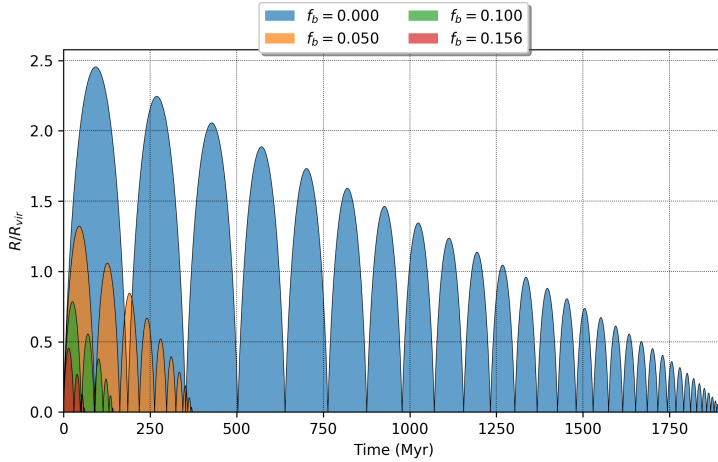


FIGURE 3.2: Effect of the baryonic fraction in the orbit of the black hole.

Three factors need to be taken into account to explain these results. First, dynamical friction due to collisional matter has an important impact on the trajectories followed by the black hole, as can be seen with the green line of Figure 3.1 (a_{DF}). Second, as there is no baryonic mass to accrete, the black hole does not decrease its speed because of momentum conservation, thus there is no contribution to the black hole's acceleration of the third term in Equation 2.14. Lastly, as seen in Figure 2.3 at short distances, the cumulative mass of the galaxy is governed by stars, from which it is expected for the black hole to reach further regions of space if there are no stars, because of the smaller potential.

1.2 Effect of the power law exponent

Many studied galaxies have luminosity profiles that follow a power law in distance. Nevertheless, power law density profiles have the exponent n as free parameter, although it is expected to be approximate to 2, as rotation curves of galaxies at large radii, show that the rotation speed of stars becomes independent of their distance to the center [15]. This can be shown by considering a system in which density drops with radius as a function of a n power:

$$\rho(r) = \rho_0^{\text{gas}} \left(\frac{r_0}{r} \right)^n \quad (3.1)$$

Hydrostatic equilibrium between the outward pressure of the galactic gas and the inward gravity from an spherical galaxy can be written as:

$$\frac{dp(r)}{dr} = -\rho(r) \frac{GM(r)}{r^2} = -\left[\rho_0^{\text{gas}} \left(\frac{r_0}{r}\right)^n\right] \frac{GM(r)}{r^2} = -\rho_0^{\text{gas}} r_0^n GM(r) r^{2-n} \quad (3.2)$$

Stationary case comes if $n = 2$, as $dp(r)/dr = 0$, whenever this happens, pressure becomes independent of r . Nevertheless, as [Equation 3.2](#) reveals, the value of n strictly depends in the force generated by gravity, which in turn depends in the mass distribution within the galaxy. By taking the gradient of the potentials on [Table B.1](#), one can see that the NFW and Hernquist profiles, generate forces almost but not equally proportional to r^{-2} .

Moreover, many galaxies show a smooth transition between two distinct power laws, one for small radii, and another one for large distances [15]. The general form for densities following a double power law is:

$$\rho(r) = \frac{\rho_0}{\left(\frac{r}{a}\right)^\alpha \left(1 + \frac{r}{a}\right)^{\beta-\alpha}} \quad (3.3)$$

From which, one obtains all of the densities profiles used, as NFW is a double power law with $(\alpha, \beta) = (1, 3)$, Hernquist $(1, 4)$ and for gases, $(0, n)$, as seen in equations [2.4](#), [2.10](#) and [2.13](#). Double power laws have an advantage over piecewise-defined functions, as they are smooth for all distances.

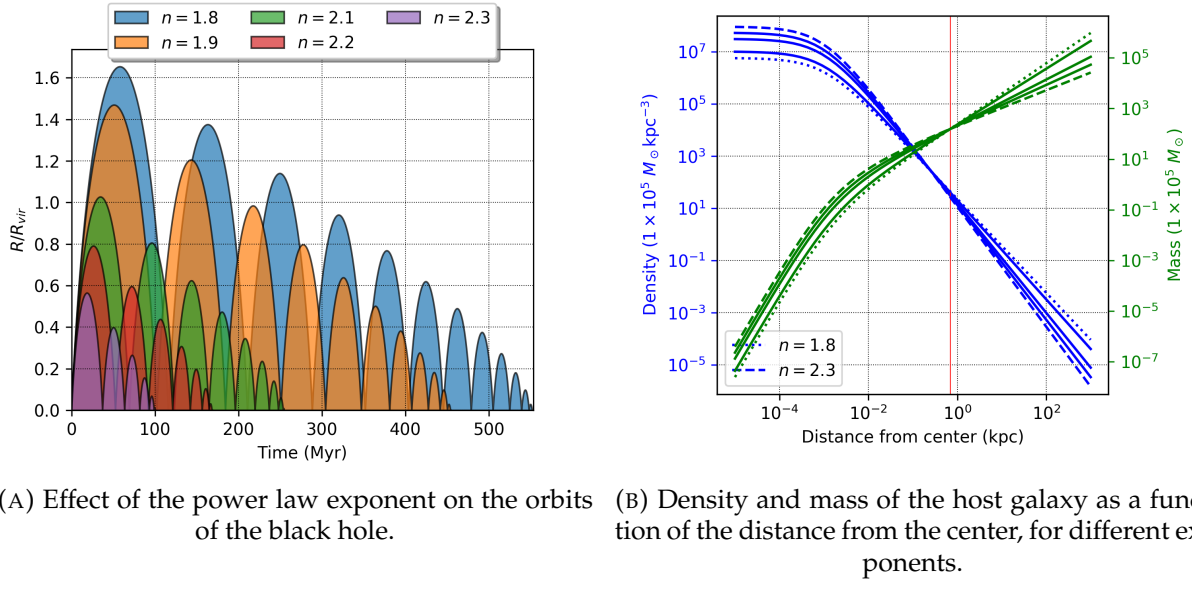


FIGURE 3.3: Properties of the power law exponent.

Since n is not fixed, simulations were made for a range of exponents in the power law. Results can be seen in [Figure 3.3](#), were a clear influence of the exponent can be seen. A confirmation that everything went the way it is supposed to, is that cumulative masses for all of the exponents have the same value at the virial radius (red line in [Figure 3.3b](#)). At this same

distance, the behavior of the mass for each exponent changes, as smaller values of n have a bigger cumulative masses from there on. At any other point, the density for bigger values of n is greater, which means that both dynamical friction and accretion rates increase for the black hole as n get bigger. Also, as n becomes greater, cumulative masses increase, yielding a higher gravitational potential. Both of these effects, take part in the observed results in [Figure 3.3a](#), in which, higher values of n increase return times.

There are some spiral galaxies from which an exponent of 2.6 has been calculated as in NGC 253 [19], others authors have made simulations for black hole escape velocities with $n = 2.2$ [7, 9]. It is from these references, from which the value of $n = 2.2$ for most simulations was selected.

1.3 Effect of the stellar fraction

As it was mentioned before, the mass of a galaxy at low distances from its center, is ruled by the amount of stars. Because of this, a study of the dependence of the return times with stellar fraction, and initial speed was carried on. For that, simulations with initial speeds from 55 to 90 kpc/Gyr were lunched, for stellar fractions ranging from 1 % to 10 %. In order to normalize speeds, initial speeds are divided by the escape velocity. By considering the potential energy at the edge of the galaxy, and the initial energy of the black hole, the escape velocity is written as:

$$v_{\text{escape}} = \sqrt{2 (\Phi(R_{\text{vir}}) - \Phi(r_0))} \quad (3.4)$$

Results from the simulations can be seen on [Figure 3.4](#), where a linear behavior below the escape speed is common for all stellar fractions. As the initial velocities approximate 1.3, an exponential growth is seen, and return times become divergent.

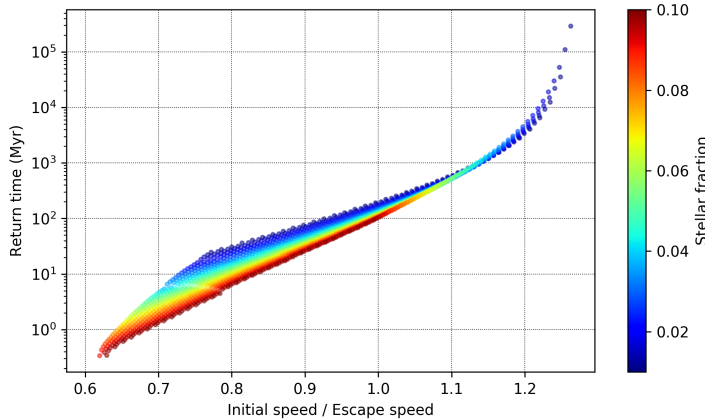


FIGURE 3.4: Return times of the black hole for different initial speeds and stellar fractions.

Return times are thus fitted to the following equation:

$$\log_{10}(T_{\text{return}}) = [a(f_s)v + b(f_s)] + \frac{c(f_s)}{v - 1.3} \quad (3.5)$$

Where the first term accounts for the linear behavior and the last for the divergence at high velocities. Using the information in [Figure 3.4](#), coefficients in [Equation 3.5](#) are calculated for each stellar fraction. Later, with the value of the coefficients, a second fit is made for $a(f_s), b(f_s), c(f_s)$.

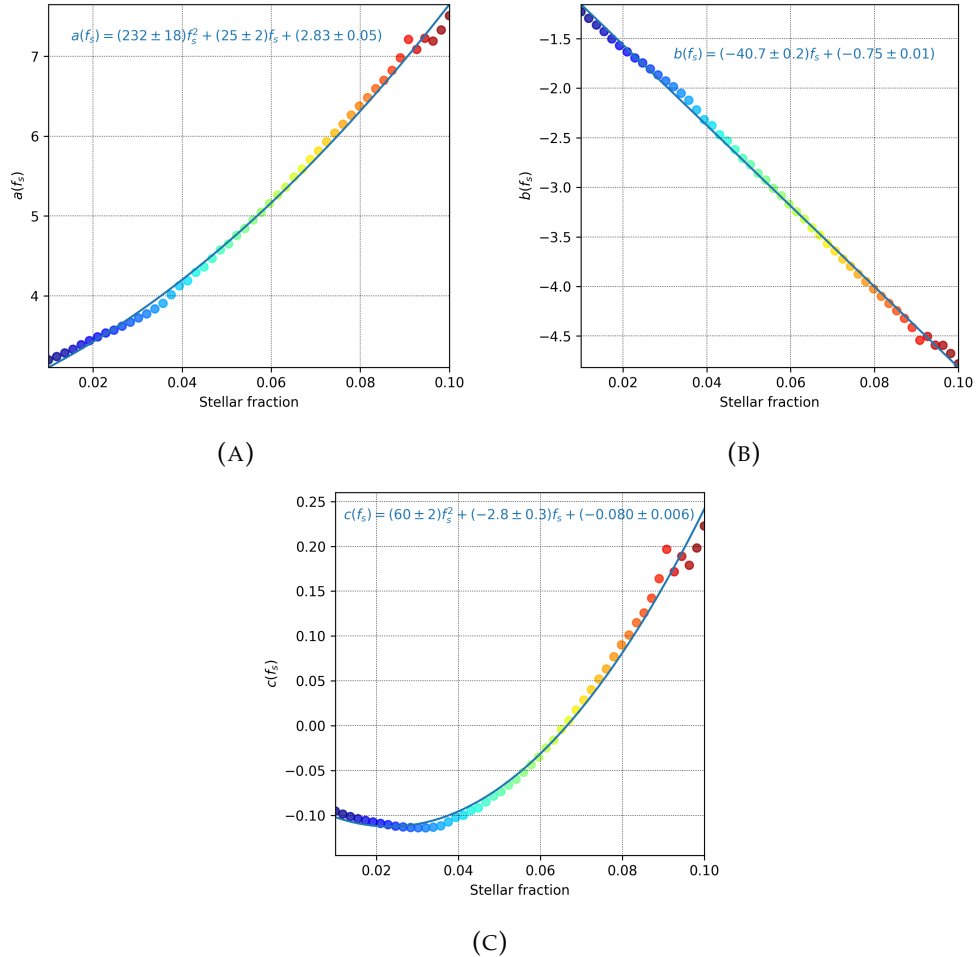


FIGURE 3.5: Fits for the coefficients in [Equation 3.5](#)

Using [Equation 3.5](#) and the fits in [Figure 3.5](#), the whole surface of return times is reconstructed, enabling the possibility of semianalytical calculations without the need of simulations, as the dependence of the coefficients with the stellar fraction is:

$$a(f_s) = 232f_s^2 + 25f_s + 2.83 \quad (3.6)$$

$$b(f_s) = -40.7f_s - 0.75 \quad (3.7)$$

$$c(f_s) = 60f_s^2 - 2.8f_s - 0.080 \quad (3.8)$$

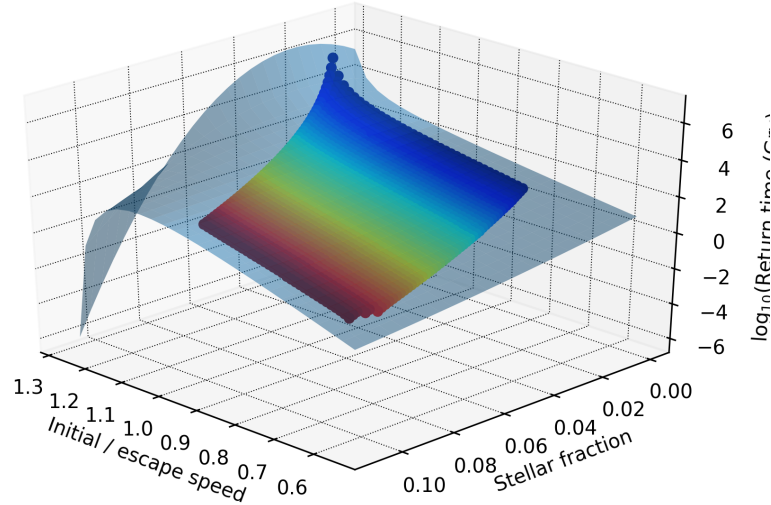


FIGURE 3.6: Constructed surface of return times of the black hole for different initial speeds and stellar fractions.

Nevertheless, as the constructed surface in Figure 3.6 shows, predicted return times for both, high stellar fractions and initial speeds, are smaller than expected.

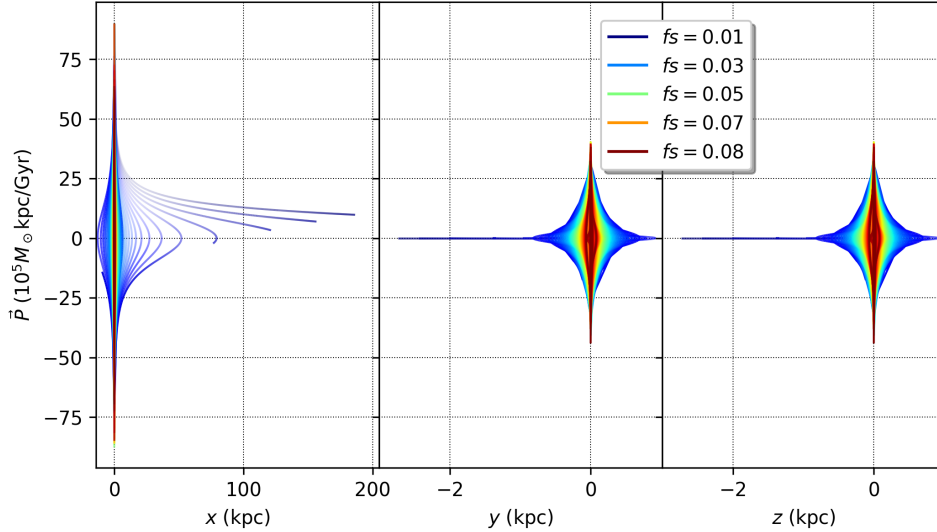


FIGURE 3.7: Phase space generated with different stellar fractions, for an initial velocity $\vec{v} = 90\hat{i} \text{kpc/Gyr}$.

On the other hand, phase spaces for high and low initial speeds, show how the increase in stellar fraction make it harder for the black hole to get further in space. In both cases, initial

velocity is only in the x direction, thus, curves in y and z happen because the initial position is not exactly $\vec{0}$, but $(1, 1, 1)$ pc, that also explains why the behavior in y and z is identical to one another.

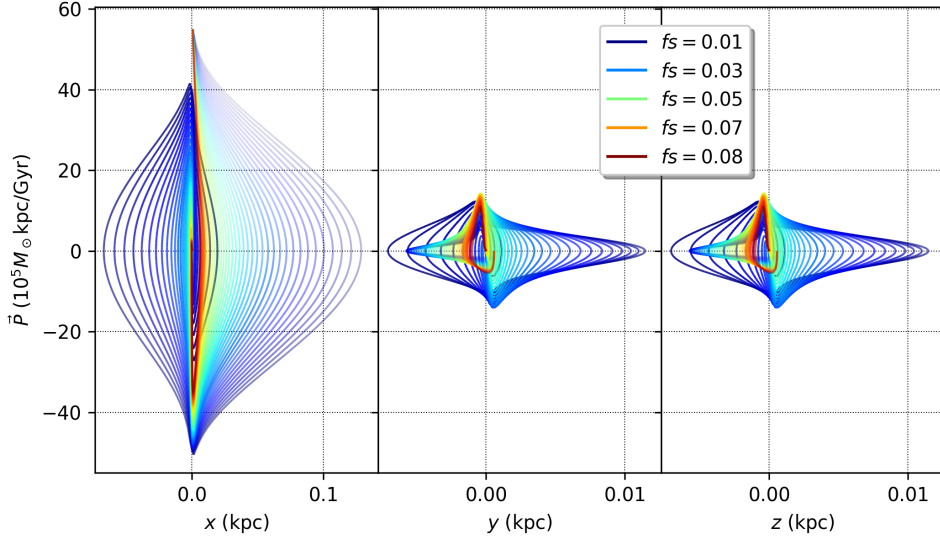


FIGURE 3.8: Phase space generated with different stellar fractions, for an initial velocity $\vec{v} = 60\hat{i}$ kpc/Gyr.

An interesting behavior in Figure 3.7 is that for the 3 smaller stellar fractions, the simulated black holes are still increasing their distance from their host galaxy as of today, while the fourth curve shows a black hole in which gravity has already overcome the initial speed, and changed the direction of the velocity.

2 Triaxial study

By using the information in Figure 3.4 relative initial speeds for the simulated galaxies were generated randomly with magnitudes ranging from $|\vec{v}_0/v_{\text{escape}}| = 0.7$ to $|\vec{v}_0/v_{\text{escape}}| = 1.2$, with random directions of the speed within the positive defined eighth of a sphere, as in Figure 3.9.

A total of 28 different pairs of semiaxis (a_2, a_3) were generated randomly using a uniform distribution. A condition was imposed for a_3 to be smaller or equal to a_2 . The distribution of the semiaxis pairs can be seen in Figure 3.10. In order to describe how close a generated galaxy is to an spherical reference, the Triaxial parameter (T) is calculated.

$$T(a_1, a_2, a_3) = \frac{1 - \left(\frac{a_2}{a_1}\right)^2}{1 - \left(\frac{a_3}{a_1}\right)^2} \quad (3.9)$$

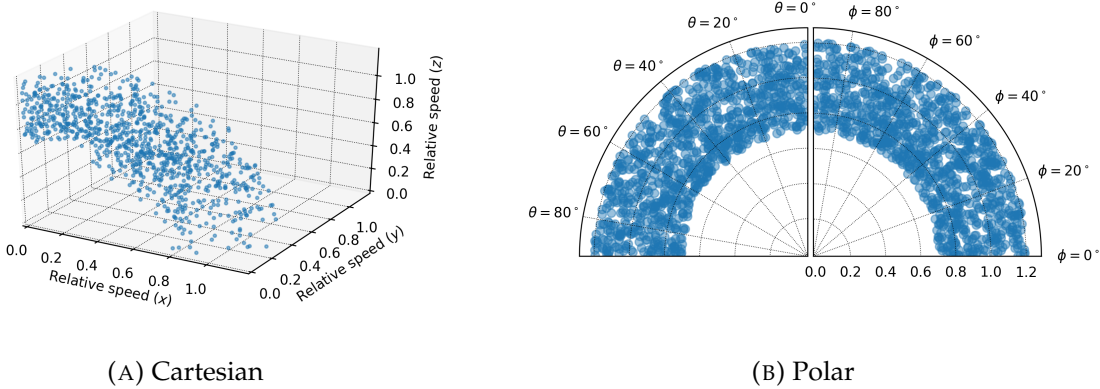


FIGURE 3.9: Distributions of initial speeds for the triaxial lunches. θ describes the polar angle and ϕ the azimuth.

Nevertheless, caution must be taken as two galaxies with the exact same T may look completely different as there are two degrees of freedom in [Equation 3.9](#). Since all values of $a_1 = 1$, the total degrees of freedom decreases to one, meaning that one pair of values of (a_2, a_3) might yield the same triaxial parameter than another pair (a'_2, a'_3) .

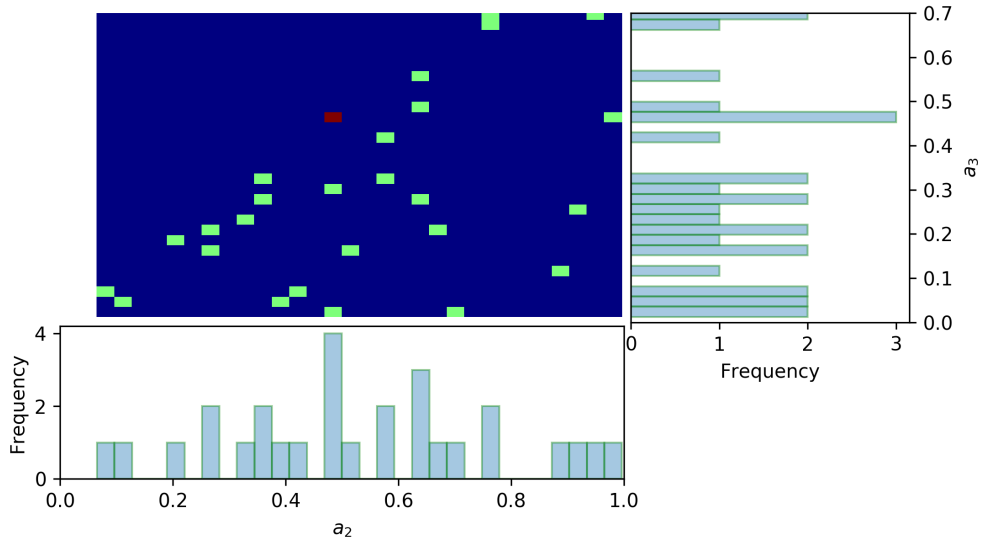
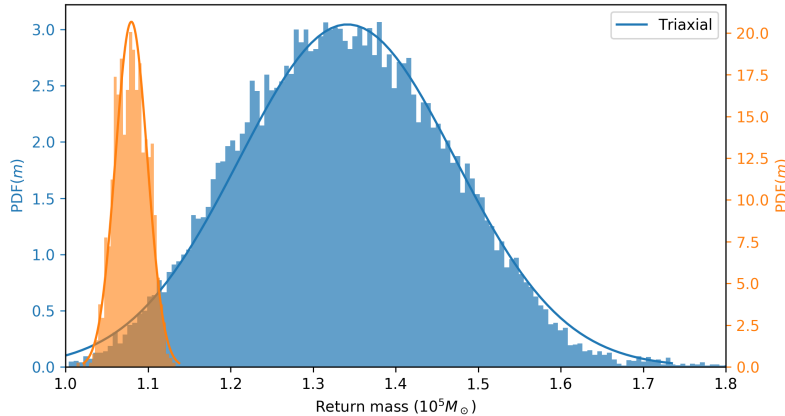


FIGURE 3.10: Distribution of the 30 pair of values for the y and z semiaxis.

2.1 Return distributions

One of the results from the 28,000 simulations is shown in [Figure 3.11](#), where the probability density for the return masses is plotted. Since results come from 28 different galaxies geometries, with triaxial parameters in the range of 9.5×10^{-3} , and 1.0, the probability densities for the return properties are independent of the galactic shapes, in fact they are considered to be an interesting statistical measurement of the overall behavior expected in the universe.



[FIGURE 3.11](#): Mass distributions of the returned black hole, for the 28 triaxial lunches (blue) and for an spherical galaxy.

[Figure 3.11](#) shows that the mass at the return time follows a gaussian Probability Density Function (PDF) given by [Equation 3.10](#), where σ^2 is variance of the data, and μ the mean.

$$\text{PDF}_{\text{Gauss}}(x, \mu, \sigma) = \frac{1}{\sqrt{2\pi\sigma^2}} e^{-\frac{(x-\mu)^2}{2\sigma^2}} \quad (3.10)$$

Both, the mean and the variance of the fitted gaussians for the distribution of return masses are shown in [Table 3.1](#), for comparison, the distribution of masses for a spherical galaxy with the same initial speeds is shown.

[TABLE 3.1](#): Parameters of the fitted gaussians in [Figure 3.11](#).

	Spherical	Triaxial
$\mu (10^5 M_\odot)$	1.08	1.34
$\sigma^2 (10^5 M_\odot)^2$	3.7×10^{-4}	1.7×10^{-2}

These results, are in concordance with previous studies, where authors argue that black holes need to be at high density areas of the galaxy, such as its center, in order to radically increase its mass by accreting material from the surroundings. One of the consequences from mass accretion is the possibility for the black hole to eventually become a quasar [9], [Table 3.1](#)

shows that on average, while a black hole experiences a kick, its mass increases only by a factor of 1.34. Quasars have masses of the order of $10^8 M_\odot$, thus it is highly difficult for a kicked black hole to become a quasar while experiencing the actual kick.

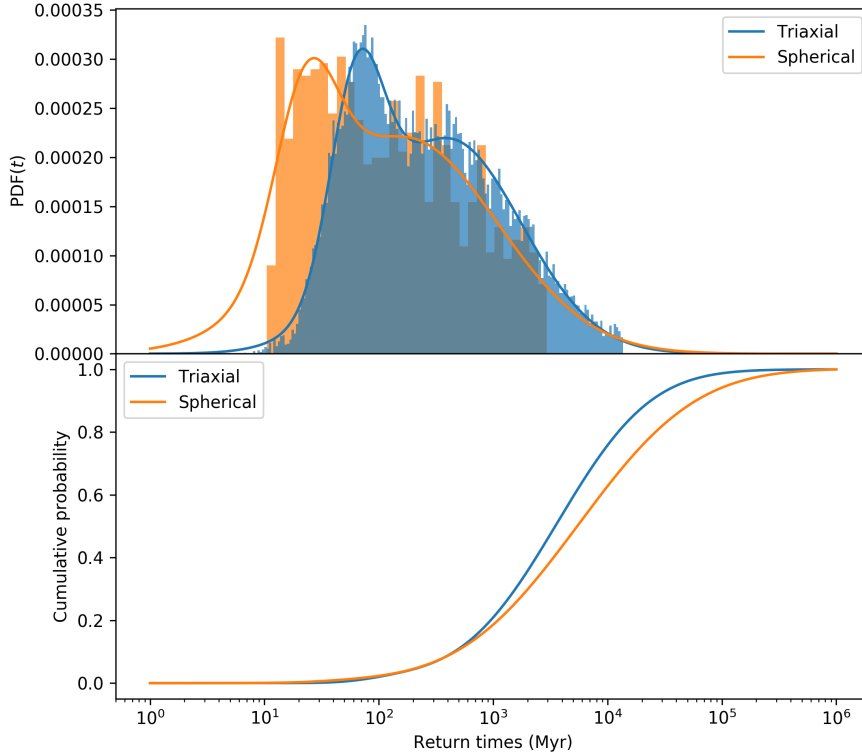


FIGURE 3.12: Return time distributions, for the 30 triaxial lunches (blue) and for an spherical galaxy. Below, the cumulative probability of the purple curve.

As for return times, they have a much wider distribution, as seen in Figure 3.12 where the data follows a logarithmic distribution. Just as with the masses, fully triaxial galaxies have higher return times when compared to an spherical galaxy. The distributions of return times are fitted to the superposition of two gaussians as described in Equation 3.11.

$$\text{PDF}(t) = \alpha \text{PDF}_{\text{Gauss}}(\log_{10} t, \mu_1, \sigma_1) + \beta \text{PDF}_{\text{Gauss}}(\log_{10} t, \mu_2, \sigma_2) \quad (3.11)$$

Additionally, with the information from the simulations the probability of finding a quasar (like ULAS J1342+0928) generated from a kicked black hole can be estimated. ULAS J1342+0928 is the furthest known quasar, it has an approximate mass of $8 \times 10^8 M_\odot$, and it is found at redshift $Z = 7.54$ [20, 21]. By considering the Λ -CDM cosmological model with the parameters described in the chapter 2, redshifts can be converted to time, for instance, redshift $Z = 7.54$ is

TABLE 3.2: Fitted values for the parameters in [Equation 3.11](#), by using [Figure 3.12](#).

	Spherical	Triaxial
$\mu_1 \log(\text{Myr})$	2.22	2.60
$\sigma_1 \log(\text{Myr})$	0.81	0.64
$\mu_2 \log(\text{Myr})$	1.36	1.81
$\sigma_1 \log(\text{Myr})$	0.27	0.23
α	4.5×10^{-4}	3.5×10^{-4}
β	1.1×10^{-4}	1.2×10^{-4}

about 692 Myr from the start of the universe, while $Z = 20$ (the redshift at which the studied black holes get a kick) is 180 Myr. This means that by evaluating the mass of all the 28,000 simulated black holes at $692 - 180 = 512$ Myr, the probability of finding a black hole with a mass of $8 \times 10^8 M_\odot$ can be calculated from the distribution of the simulated black holes masses.

2.2 Correlation between mass and time

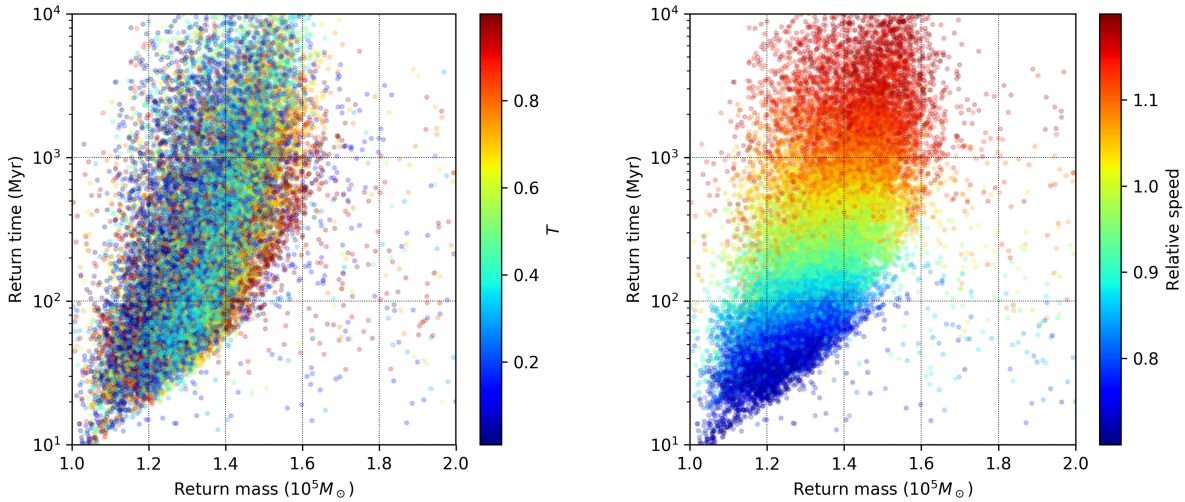
The spatial distribution of the return times, masses and Lyapunov exponents for each galaxy can be seen in the [Appendix D](#), by inspecting these results, a correlation between the return times and masses can be seen. By considering the Pearson moment of correlation, this behavior can be quantified using [Equation 3.12](#).

$$r_{\log_{10} t, m} = \frac{\text{cov}(\log_{10} t, m)}{\sigma_{\log_{10} t} \sigma_m} \quad (3.12)$$

The calculated value for all the studied orbits, of the Pearson correlation is 0.63, which is in accordance with the behavior seen in both the [Appendix D](#) and ??, describing a positive correlation between the masses and return times, that is, that an increase in the return mass most of the times will mean that the return time also increases. Furthermore, the triaxial parameter seems to change the slope in [Figure 3.13a](#), smaller T galaxies have a tendency to have higher slopes than galaxies with triaxial parameters close to the unity. Additionally, when the correlation is studied with respect to the initial speed of each black hole, horizontal zones are found, this means that the effect of the initial speed in the return mass is far less than the effect in the return time, allowing the formation of colored zones in [Figure 3.14b](#).

2.3 Triaxial vs Spherical galaxies

An important consequence of triaxial galaxies is that the magnitude of the velocity can no longer predict a unique return time, since there is a complete probability distribution associated to one value of the speed, these can clearly be seen in [Figure 3.14a](#), where a graph analogous to



(A) Colors identify the triaxial parameter of each galaxy.
 (B) Colors identify the initial relative speed of a specific return time and mass.

FIGURE 3.13: Correlation between the return times and the return masses.

[Figure 3.4](#) for the galaxies with lower and higher values of the triaxial parameter. These results are particularly important as for a single speed, depending on the direction, two very different (almost one order of magnitude) return times will be generated for the same triaxial galaxy. This same figure shows that depending on the direction of the velocity, return times for triaxial galaxies might be shorter than thus expected with using an spherical model.

As for return masses, triaxial galaxies consistently show higher values than those generated by the same initial conditions in an spherical galaxy. Nevertheless, all galaxies have a small tendency to increase its return mass with increasing initial speeds. On the other hand, caution must be taken with [Figure 3.14b](#), as mass distributions seem to be much wider than those of the return times, that is just a visual effect due to the logarithmic axis of [Figure 3.14a](#).

Despite the fact that [Figure 3.14](#) only shows results for two triaxial galaxies, an interesting behavior is found when comparing these results with those from an spherical galaxy. For small initial speeds, triaxial galaxies show higher return times than their spherical analog, while for high initial this pattern gets inverted, particularly for big T galaxies (red curves in [Figure 3.14a](#)).

As for the Lyapunov exponents it has been found that there is a dependency with the magnitude of the velocity for more spherical galaxies, in oblate galaxies the behavior of the return properties is controlled by the z component of the initial speed.

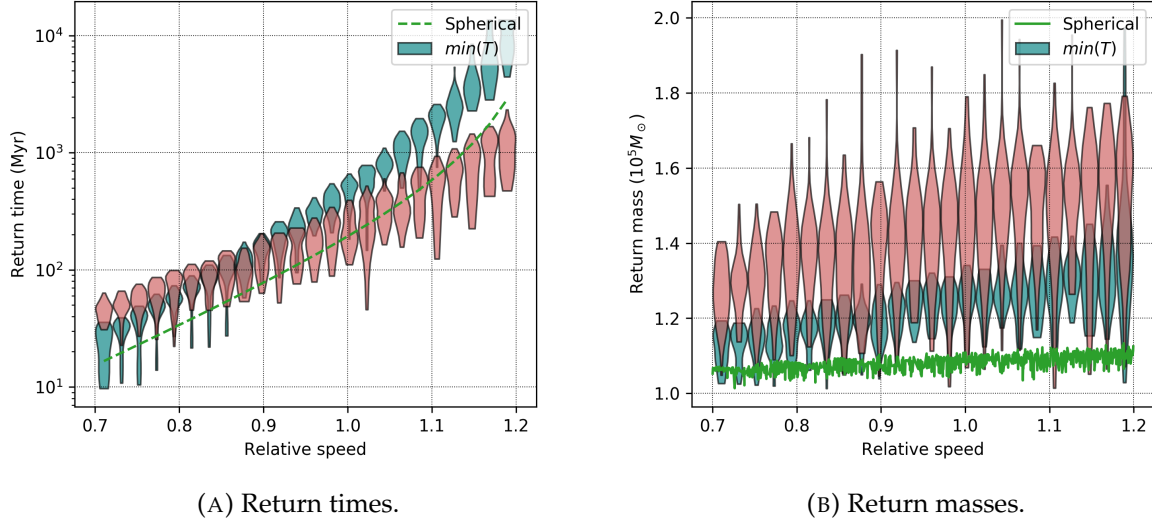


FIGURE 3.14: Probability distributions for the galaxies with higher and lower (red and blue) triaxial parameters, for the return properties as a function of the initial speed.

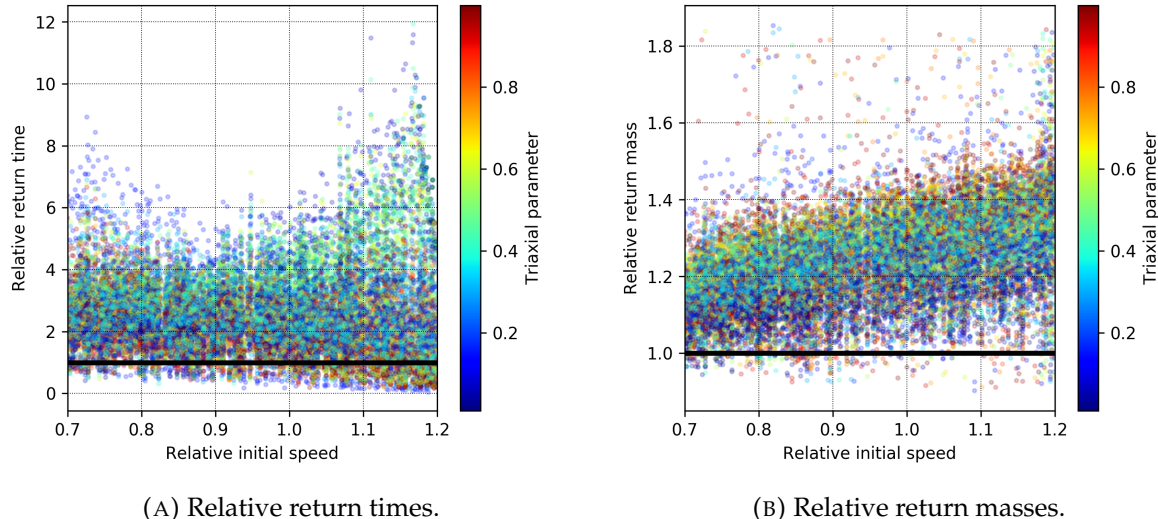


FIGURE 3.15: Relative distribution of the return properties as a function of the initial speed.

Chapter 4

Conclusions

Appendix A

Computational setup

1 Units

Computer simulations are sensitive to rounding errors due to the lack of infinite precision when representing decimal numbers. Really small numbers as well as really big ones tend to have bigger errors than those close to the unity, as can be seen on [Figure A.1](#).

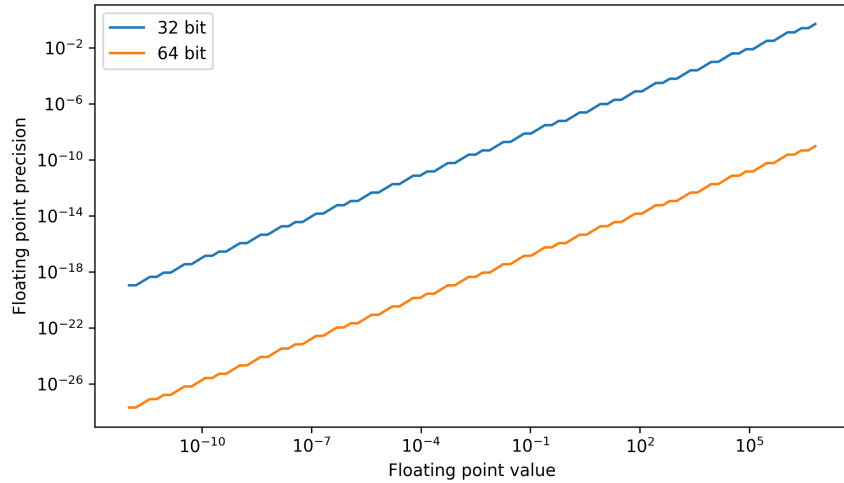


FIGURE A.1: Floating point precision for different values, for a 32 bit and 64 bit holders.

Under the International System of Units, distances are measured on meters, times on seconds, and masses on kilograms, nevertheless black holes are too heavy to be measured on kilograms, galaxies sizes too big to be quantified on meters, and time scales too large for a second. Because of that, the following units will be used throughout this document:

Along with the change of units, the universal gravitational constant and the Hubble parameter values are required to change.

TABLE A.1: Units of measure used on the simulations.

Physical property	unit
Length	1 kilo-parsec (kpc)
Mass	10^5 solar masses ($10^5 M_\odot$)
Time	1 giga-year (Gyr)

1.1 Universal gravitational constant

First quantified by Henry Cavendish the gravitational constant has a value of $G_0 = 6.67408 \times 10^{-11}$ on SI units of $\text{m}^3\text{s}^{-2}\text{kg}^{-1}$. With the units of length, mass and time on Table A.1, the constant of gravity used is given by:

$$\begin{aligned} G &= G_0 \left(\frac{1 \text{ kpc}^3}{(3.0857 \times 10^{19})^3 \text{ m}^3} \right) \left(\frac{(3.154 \times 10^{16})^2 \text{ s}^2}{1 \text{ Gyr}^2} \right) \left(\frac{1.98847 \times 10^{35} \text{ kg}}{10^5 M_\odot} \right) \\ &= 0.4493 \frac{\text{kpc}^3}{\text{Gyr}^2 10^5 M_\odot} \end{aligned} \quad (\text{A.1})$$

1.2 Hubble parameter

The Hubble constant is frequently used as $H_0 = 67.66 \pm 0.42 \text{ kms}^{-1}\text{Mpc}^{-1}$ [22], stating the speed of an astronomical body on kms^{-1} at a distance of 1 Mpc. Nevertheless, the hubble constant has units of 1/time, thus, taking into account the units on Table A.1 one gets:

$$\begin{aligned} H &= H_0 \left(\frac{1 \text{ kpc}}{3.0857 \times 10^{16} \text{ km}} \right) \left(\frac{3.154 \times 10^{16} \text{ s}}{1 \text{ Gyr}} \right) \left(\frac{1 \text{ Mpc}}{1000 \text{ kpc}} \right) \\ &\approx 1.023 H_0 \times 10^{-3} \text{ Gyr}^{-1} \\ &= 6.916 \times 10^{-2} \text{ Gyr}^{-1} \end{aligned} \quad (\text{A.2})$$

Although the Hubble parameter is often called Hubble constant, its value changes with time as can be seen on Figure A.2.

2 Critical density and Virial Radius

Mass distributions used for the simulation of the host galaxy, are divergent for distances up to infinity. Because of this, the cumulative mass of all bodies within a given distance is called the virial mass and its value is taken as the mass of the whole system. The distance taken to calculate the virial mass is called virial radius (R_{vir}), and it is defined as the distance at which

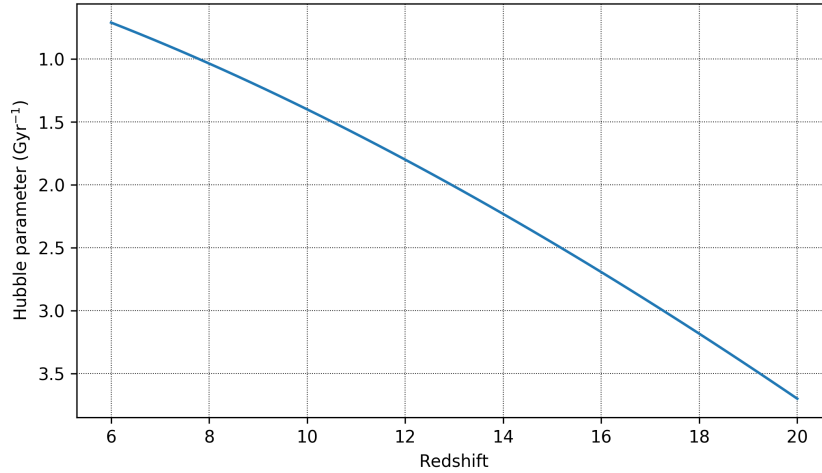


FIGURE A.2: Dependency of the Hubble parameter with redshift.

the average density of the galaxy is 200 times the critical density of the universe (ρ_{crit}).

$$\rho_{\text{crit}} = \frac{3H(t)^2}{8\pi G} \quad (\text{A.3})$$

$$\frac{M(R_{\text{vir}})}{V(R_{\text{vir}})} = \bar{\rho}(R_{\text{vir}}) = 200\rho_{\text{crit}} = 75 \frac{H(t)^2}{\pi G} \quad (\text{A.4})$$

where $M(R_{\text{vir}})$ is the cumulative mass, and $V(R_{\text{vir}})$: the volume

The relation on [Equation A.3](#) is found by considering the case where the geometry of the universe is flat, as a consequence it is said that the critical density is the minimum density required to stop the expansion of the universe [\[15\]](#).

Appendix B

Time integration

Although [Equation 2.14](#) is a one body equation of motion, it is a second order differential equation with no analytical solution due to the complexity of the gravitational and dynamical friction components. Thus, to evolve the position of the black hole in time, numerical integration of the equation is carried on using the Leapfrog method.

Graphically the differential equation is integrated in three steps, as seen on [Figure B.1](#). First, from the acceleration at the current position i , a mid-point velocity is found ($\vec{v}_{i+1/2}$). With this velocity, the position at the next time step is calculated. Finally, the velocity at $i + 1$ is found using the acceleration at this spot.

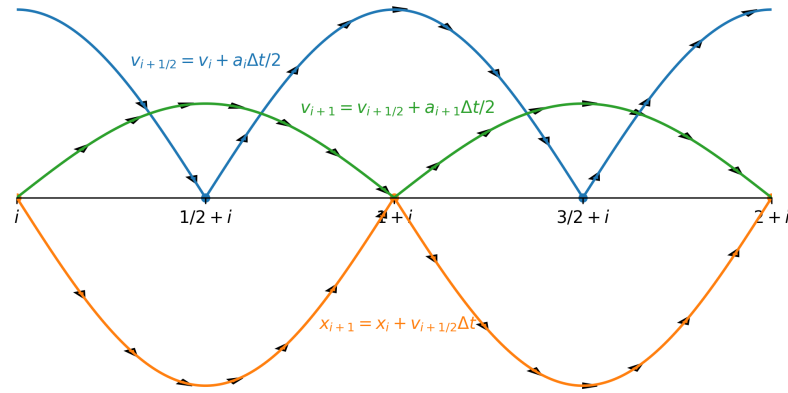


FIGURE B.1: Leapfrog integration scheme

These steps are shown on [Equation B.1](#) to [Equation B.3](#), where $a_i \equiv \ddot{\vec{x}}(\vec{x}_i, \dot{\vec{x}}_i)$ from [Equation 2.14](#), and $\dot{\vec{x}}_i \equiv \vec{v}_i$.

$$\vec{v}_{i+1/2} = \vec{v}_i + \vec{a}_i \left(\frac{\Delta t}{2} \right) \quad (\text{B.1})$$

$$\vec{x}_{i+1} = \vec{x}_i + \vec{v}_{i+1/2} \Delta t \quad (\text{B.2})$$

$$\vec{v}_{i+1} = \vec{v}_{i+1/2} + \vec{a}_{i+1} \left(\frac{\Delta t}{2} \right) \quad (\text{B.3})$$

Since the Leapfrog integration scheme, does not yield an analytical solution, it is sensitive to numerical errors. Because of this, an error assessment is done comparing the energy for nondissipative simulations, for both, the spherical and triaxial cases ($a_1 = a_2 = a_3 = 1$). By removing the second term on [Equation 2.14](#), stable orbits are found, and energy should be conserved. From the first law of thermodynamics, conservation of energy is given by:

$$E_T = K + V = \frac{1}{2}m_0 v_0^2 + m_0 \Phi_{\text{grav}}^0 = \frac{1}{2}m_i v_i^2 + m_i \Phi_{\text{grav}}^i \quad (\text{B.4})$$

The gravitational potential is the sum of the potential generated by dark matter (Φ_{DM}), stars (Φ_{stars}) and gas (Φ_{gas}) at a distance r .

TABLE B.1: Φ values for the studied density profiles

Profile	$\Phi(r)$
NFW	$-\frac{4\pi G \rho_0^{\text{DM}} R_s^3}{r} \ln \left(1 + \frac{r}{R_s} \right)$
Hernquist	$-\frac{G f_s f_b M_h}{r + R_s}$
Power-law	$-\frac{4\pi G \rho_0^{\text{gas}} (r+r_0)^{-n} (2nr^2 r_0^{n+4} + r^3 r_0^{n+3} (n-1) + rr_0^{n+5} (n+3) - 2r_0^6 (r+r_0)^n + 2r_0^{n+6})}{rr_0^3 (n-3)(n-2)(n-1)}$

To check for energy changes over time, a total of 106 orbits were made, following [Poon and Merritt](#). These simulations lasted for almost half the age of the universe.

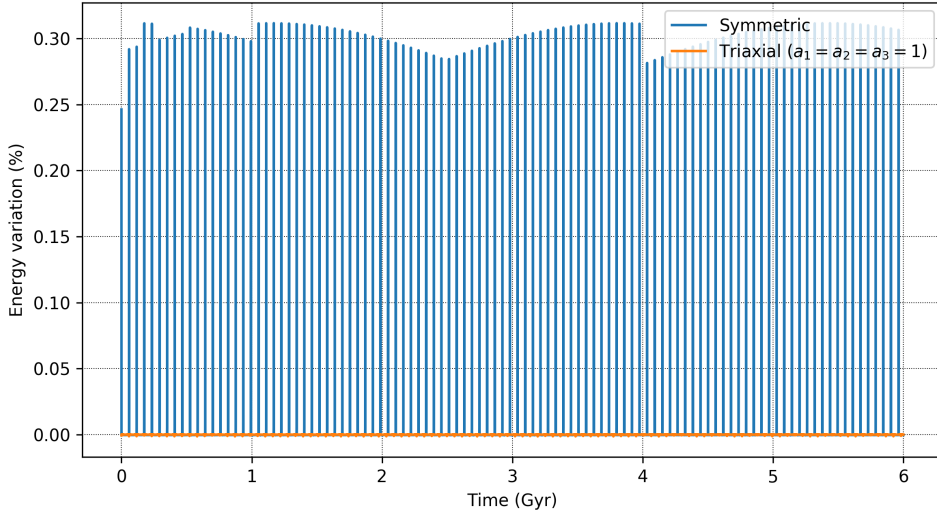


FIGURE B.2: Energy variations of the Leapfrog scheme

Figure B.2 shows a maximum fluctuation for the spherical case of 0.312 % after more than a hundred dynamical times, while for the triaxial case oscillations are much smaller with a maximum amplitude of 0.001 %. Despite the local changes in energy, energy is conserved globally using the Leapfrog scheme.

Appendix C

Lyapunov exponents

In chaotic behavior, infinitesimally close initial conditions lead to evolutions that diverge exponentially fast. The Maximum Lyapunov Exponent \mathcal{L} , is an indicative of the rate of such divergence [24].

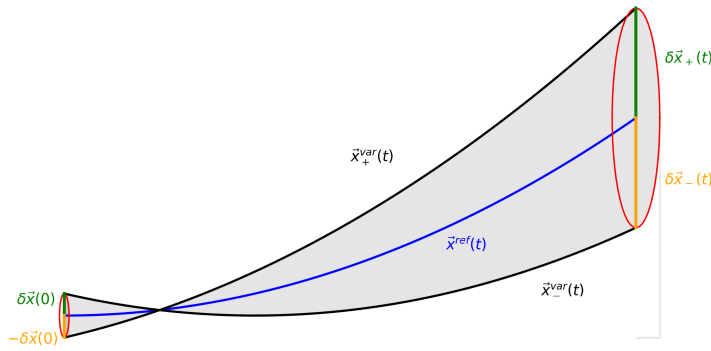


FIGURE C.1: Representation of three arbitrary close orbits, and their evolution in time.

Consider the upper two orbits (\mathcal{O}^{ref} , \mathcal{O}^{var}) in Figure C.1, with initial conditions $\vec{x}^{\text{ref}}(0)$, $\vec{p}^{\text{ref}}(0)$ and $\vec{x}^{\text{var}}(0)$, $\vec{p}^{\text{var}}(0)$. Denoting the distance in each of the components of the phase space as:

$$\delta\vec{x}(t) = \vec{x}^{\text{ref}}(t) - \vec{x}^{\text{var}}(t) = (x^{\text{ref}}(t) - x^{\text{var}}(t), y^{\text{ref}}(t) - y^{\text{var}}(t), z^{\text{ref}}(t) - z^{\text{var}}(t)) \quad (\text{C.1})$$

$$\delta\vec{p}(t) = \vec{p}^{\text{ref}}(t) - \vec{p}^{\text{var}}(t) = (p_x^{\text{ref}}(t) - p_x^{\text{var}}(t), p_y^{\text{ref}}(t) - p_y^{\text{var}}(t), p_z^{\text{ref}}(t) - p_z^{\text{var}}(t)) \quad (\text{C.2})$$

the Maximum Lyapunov Exponent can be written as [24, 25]:

$$\mathcal{L} = \lim_{t \rightarrow \infty} \frac{1}{t} \ln \frac{|\delta\vec{x}(t), \delta\vec{p}(t)|}{|\delta\vec{x}(0), \delta\vec{p}(0)|} \quad (\text{C.3})$$

where $|\delta\vec{x}(t), \delta\vec{p}(t)|$ is the Euclidean norm of the 6 dimensional phase space. The numerical calculation of \mathcal{L} requires special care, as a computation up to infinity must be done [24]. In 1980 a technique by [Benettin et al.](#) solved this problem, as The Maximum Lyapunov Exponent can be calculated as follows:

1. Define an arbitrary initial distance in the phase space $\delta\vec{x}(0) = (\delta x_0, \delta y_0, \delta z_0), \delta\vec{p}(0) \equiv 0$.
2. Simulate both \mathcal{O}^{ref} and \mathcal{O}^{var} until a predefined time T .
3. Calculate the distance in phase space at time T between the reference orbit and the variational one (equations C.1 and C.2).
4. Calculate the coefficient s_i .

$$s_i = \frac{|\delta\vec{x}_i(T), \delta\vec{p}_i(T)|}{|\delta_i\vec{x}(0), \delta_i\vec{p}(0)|} \quad (\text{C.4})$$

5. For the new iteration, $\delta_{i+1}\vec{x}(0) = \delta_i\vec{x}(T)/s_i$, and $\delta_{i+1}\vec{p}(0) = \delta_i\vec{p}(T)/s_i$
6. Repeat l times, to obtain:

$$\mathcal{L} = \frac{\sum_{i=1}^l \ln(s_i)}{lT} \quad (\text{C.5})$$

To illustrate the concept of initial and final separation, in [Figure C.2](#) the lunches of 7 simulations with initial conditions $(x \pm \delta, y, z)$, $(x, y \pm \delta, z)$, $(x, y, z \pm \delta)$ and (x, y, z) are plotted.

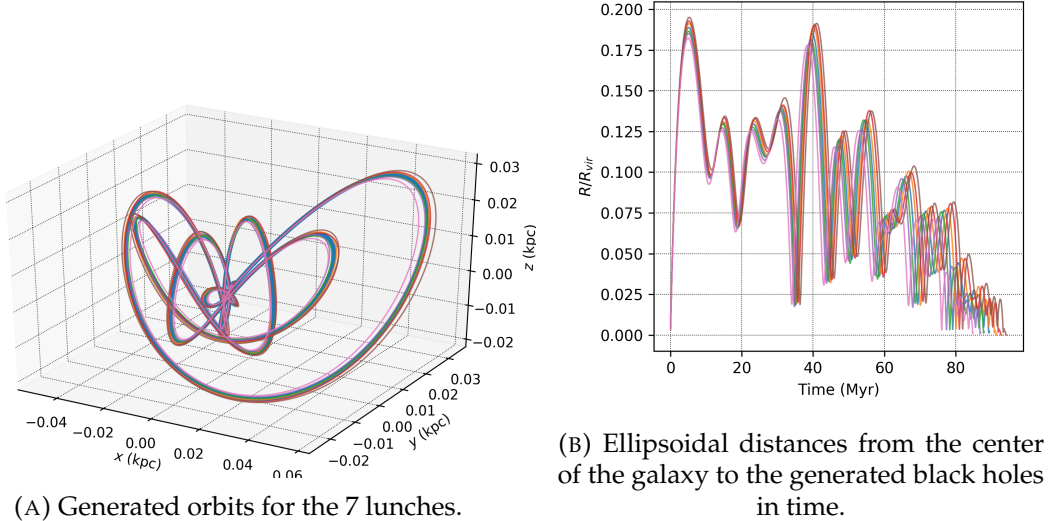


FIGURE C.2: Separation in time between orbits with initial distances of $\delta = 1 \times 10^{-4}$ kpc.

Appendix D

Triaxial Galaxies

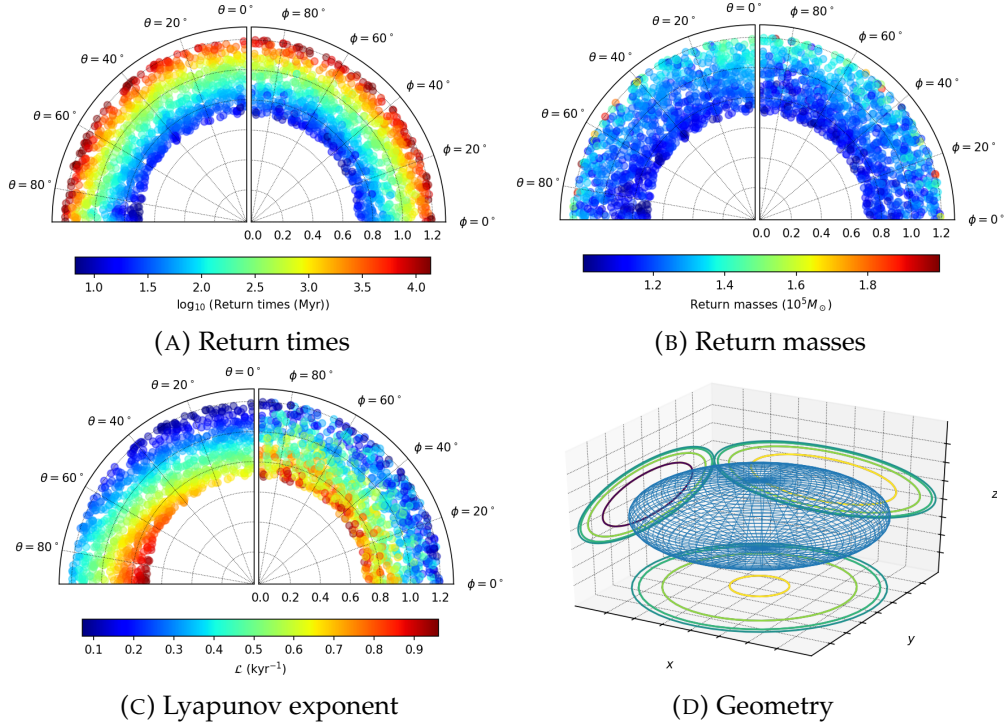


FIGURE D.1: Distribution of the different properties for the galaxy with $a_1 = 1$, $a_2 = 1.0e + 00$, $a_3 = 4.6 \times 10^{-1}$.

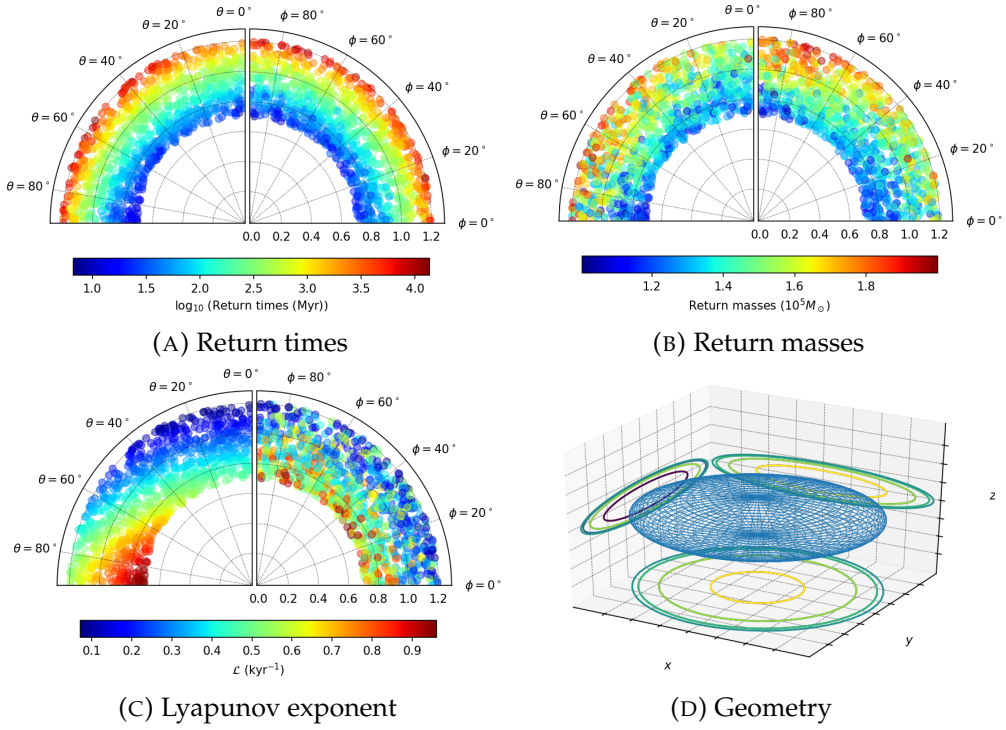


FIGURE D.2: Distribution of the different properties for the galaxy with $a_1 = 1$, $a_2 = 9.3 \times 10^{-1}$, $a_3 = 2.6 \times 10^{-1}$.

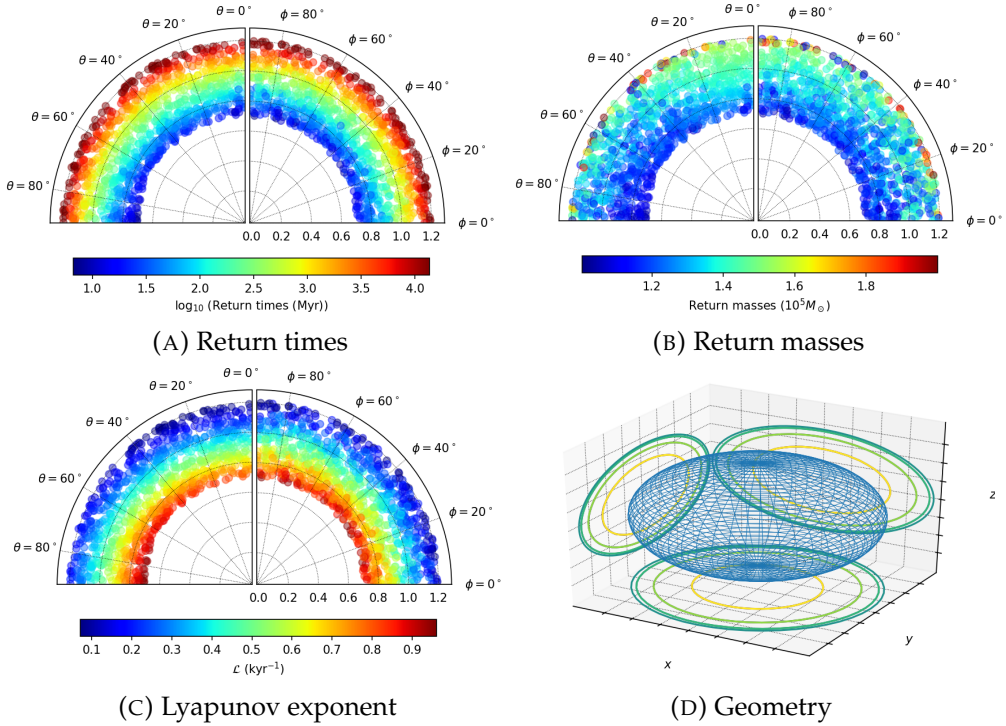


FIGURE D.3: Distribution of the different properties for the galaxy with $a_1 = 1$, $a_2 = 9.6 \times 10^{-1}$, $a_3 = 7.0 \times 10^{-1}$.

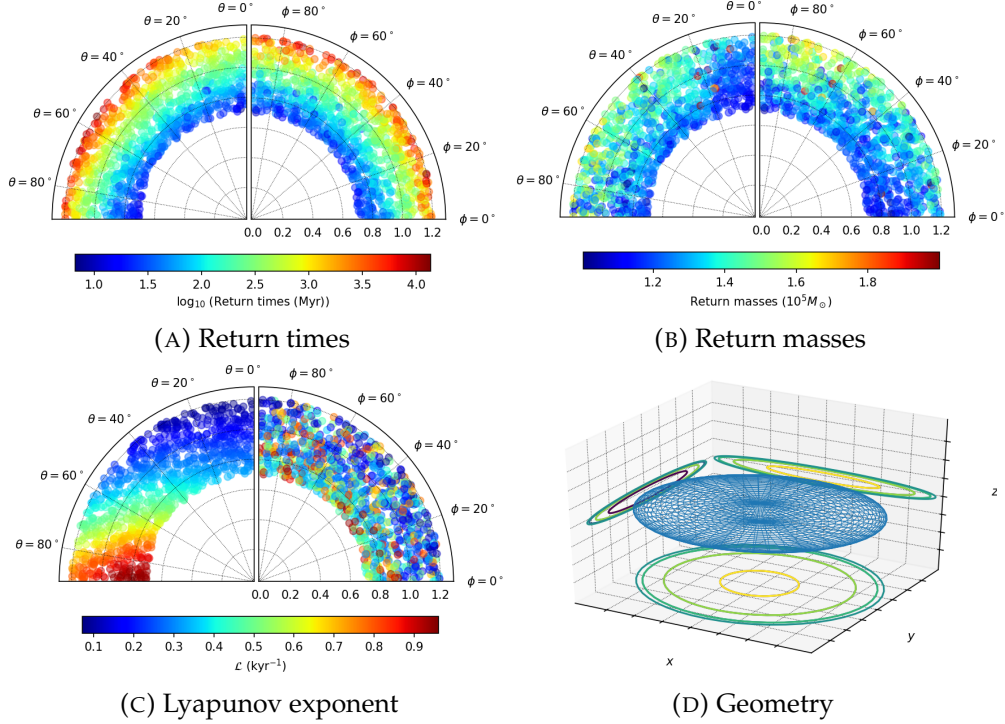


FIGURE D.4: Distribution of the different properties for the galaxy with $a_1 = 1$, $a_2 = 8.7 \times 10^{-1}$, $a_3 = 1.3 \times 10^{-1}$.

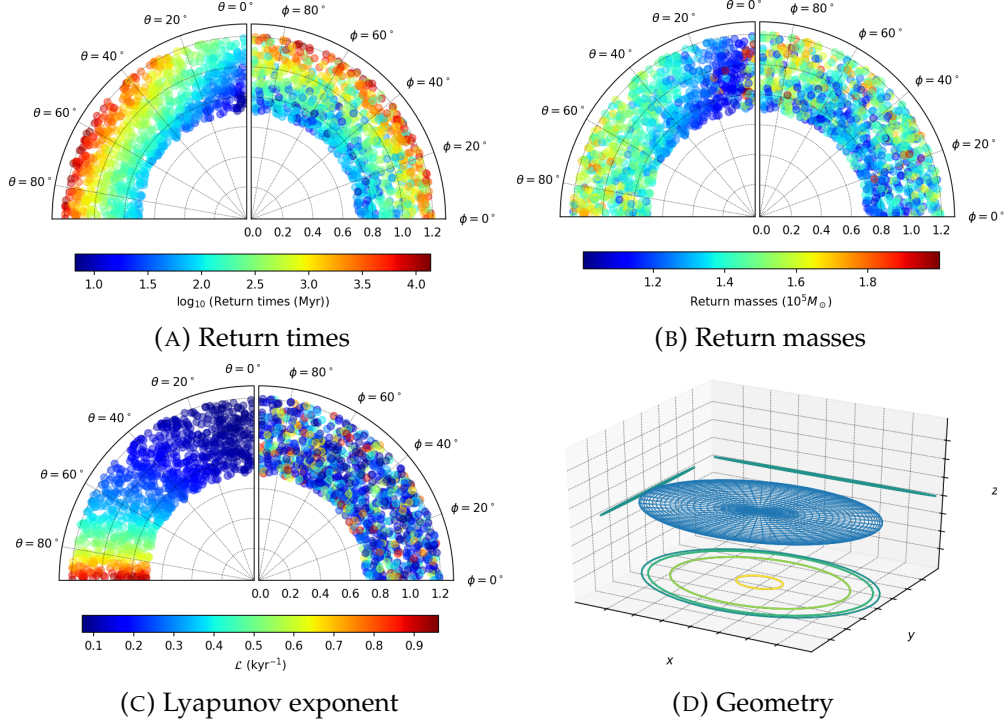


FIGURE D.5: Distribution of the different properties for the galaxy with $a_1 = 1$, $a_2 = 6.9 \times 10^{-1}$, $a_3 = 1.2 \times 10^{-2}$.

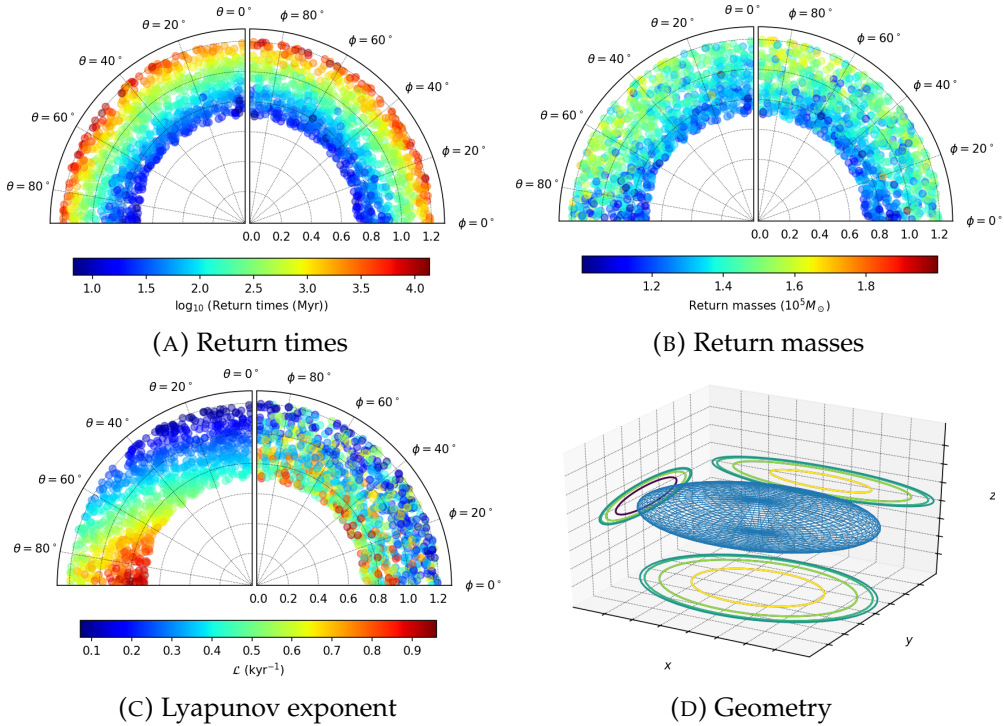


FIGURE D.6: Distribution of the different properties for the galaxy with $a_1 = 1$, $a_2 = 6.8 \times 10^{-1}$, $a_3 = 2.2 \times 10^{-1}$.

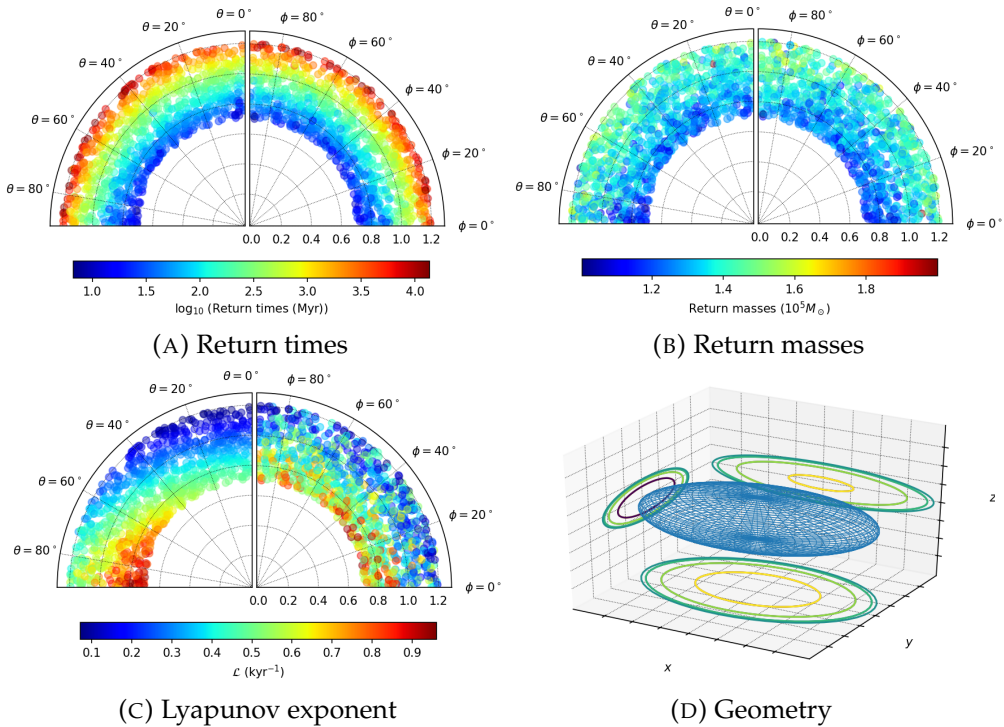


FIGURE D.7: Distribution of the different properties for the galaxy with $a_1 = 1$, $a_2 = 6.3 \times 10^{-1}$, $a_3 = 2.8 \times 10^{-1}$.

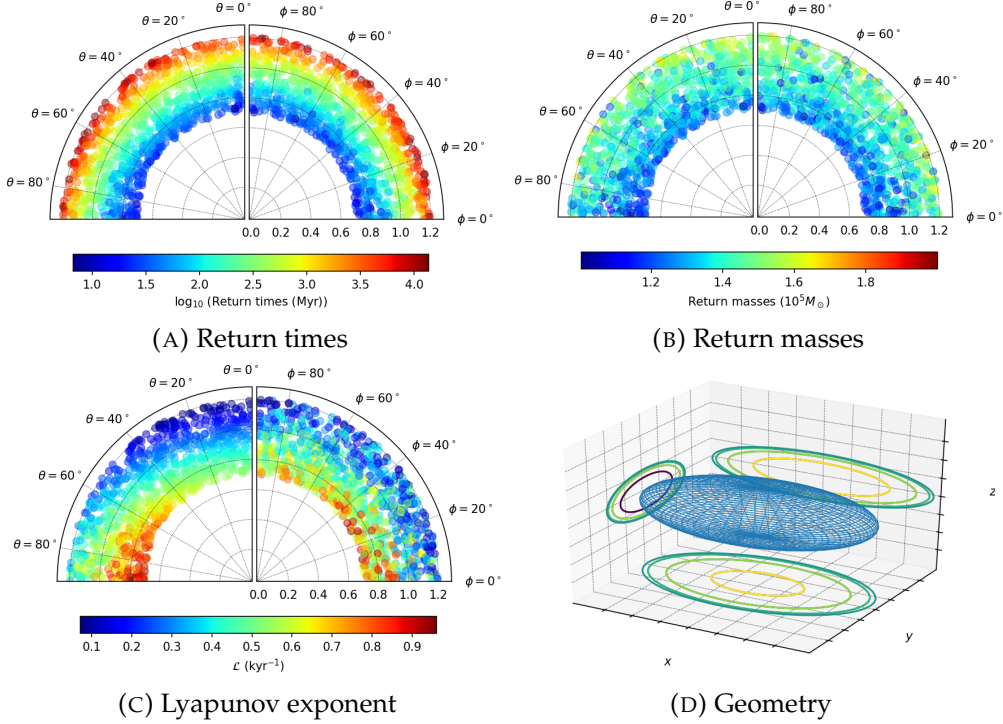


FIGURE D.8: Distribution of the different properties for the galaxy with $a_1 = 1$, $a_2 = 5.7 \times 10^{-1}$, $a_3 = 3.3 \times 10^{-1}$.

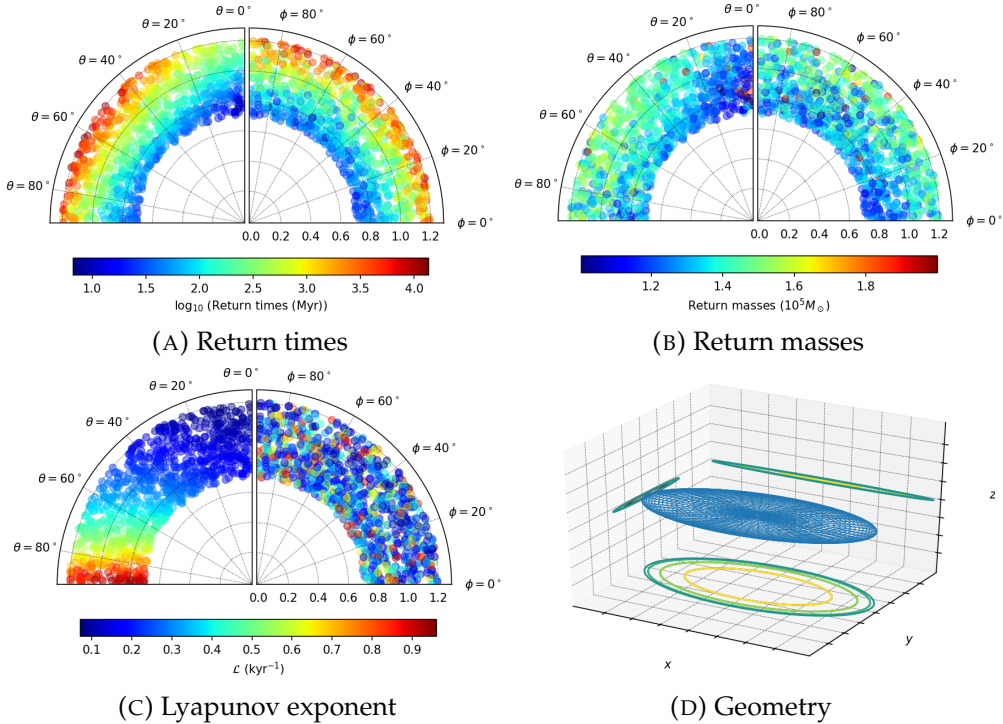


FIGURE D.9: Distribution of the different properties for the galaxy with $a_1 = 1$, $a_2 = 4.8 \times 10^{-1}$, $a_3 = 3.1 \times 10^{-2}$.

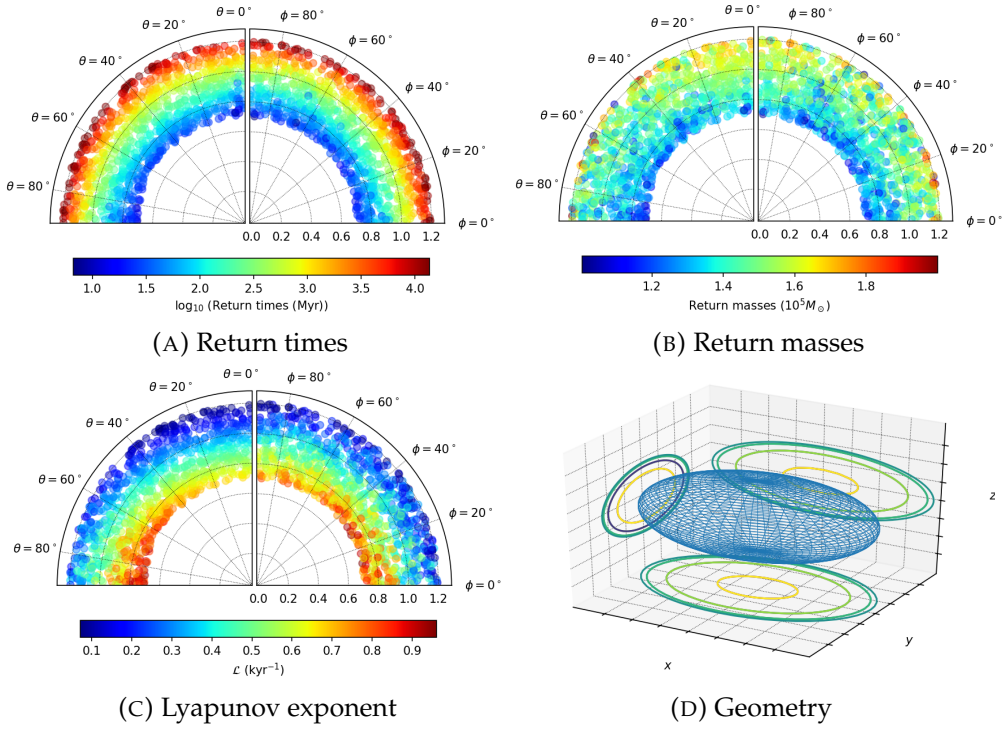


FIGURE D.10: Distribution of the different properties for the galaxy with $a_1 = 1$, $a_2 = 6.4 \times 10^{-1}$, $a_3 = 4.8 \times 10^{-1}$.

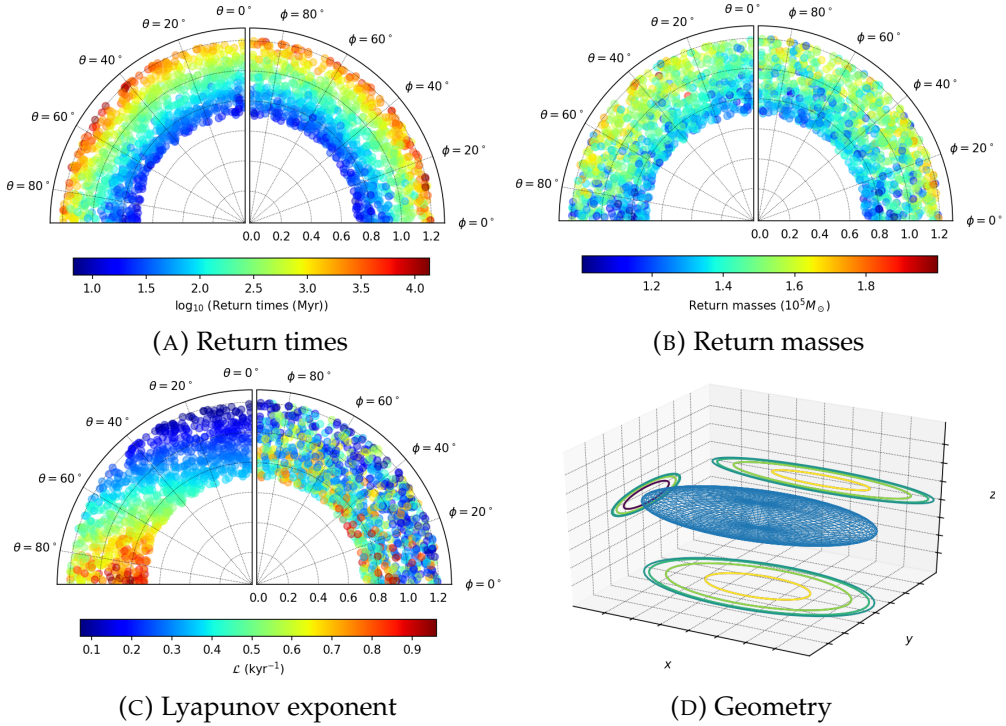


FIGURE D.11: Distribution of the different properties for the galaxy with $a_1 = 1$, $a_2 = 5.0 \times 10^{-1}$, $a_3 = 1.7 \times 10^{-1}$.

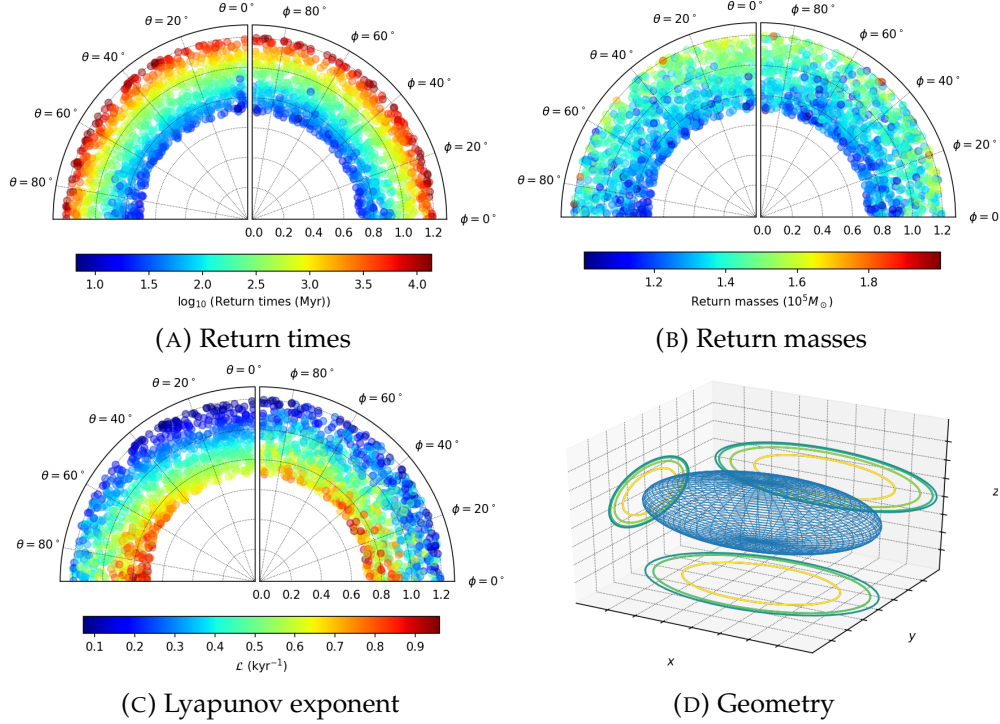


FIGURE D.12: Distribution of the different properties for the galaxy with $a_1 = 1$, $a_2 = 5.8 \times 10^{-1}$, $a_3 = 4.1 \times 10^{-1}$.

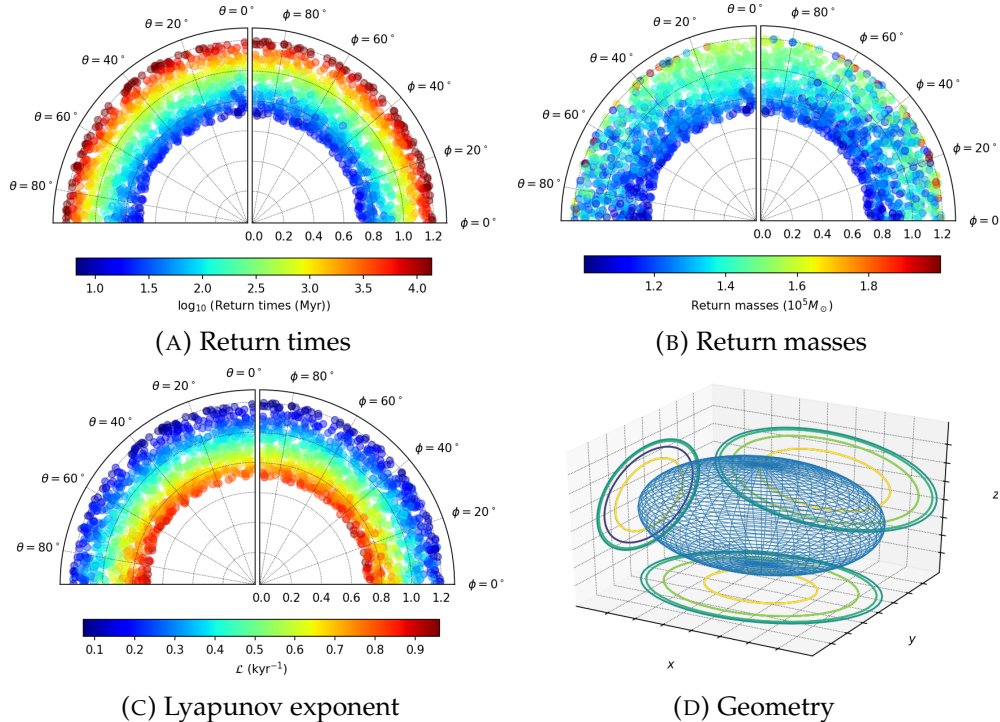


FIGURE D.13: Distribution of the different properties for the galaxy with $a_1 = 1$, $a_2 = 7.5 \times 10^{-1}$, $a_3 = 6.8 \times 10^{-1}$.

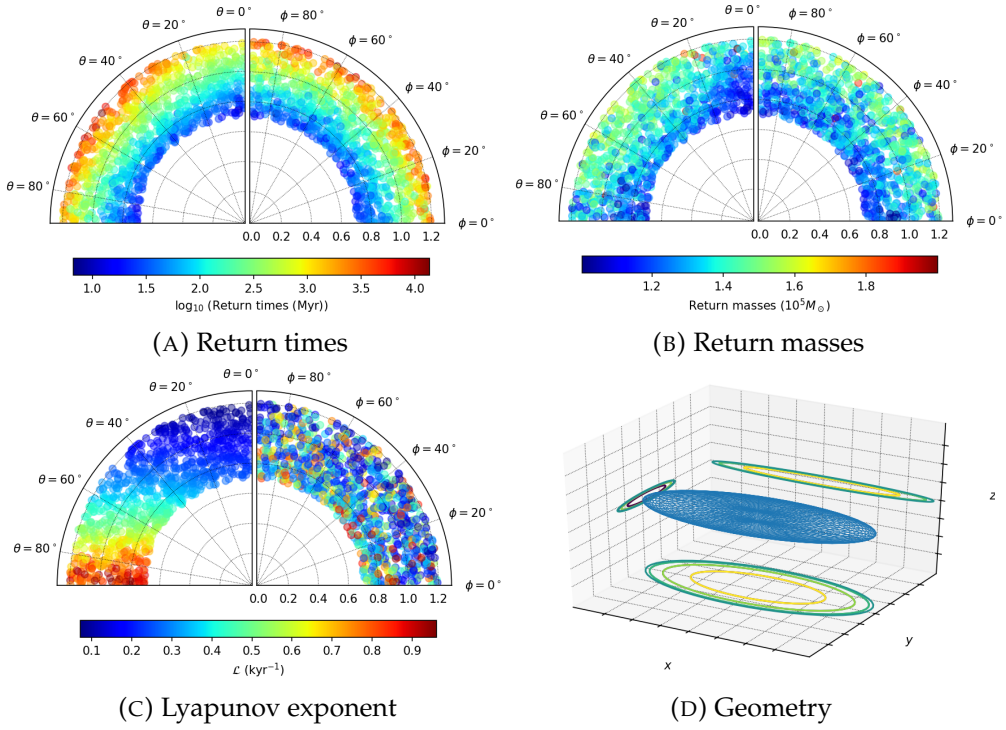


FIGURE D.14: Distribution of the different properties for the galaxy with $a_1 = 1$, $a_2 = 4.2 \times 10^{-1}$, $a_3 = 7.4 \times 10^{-2}$.

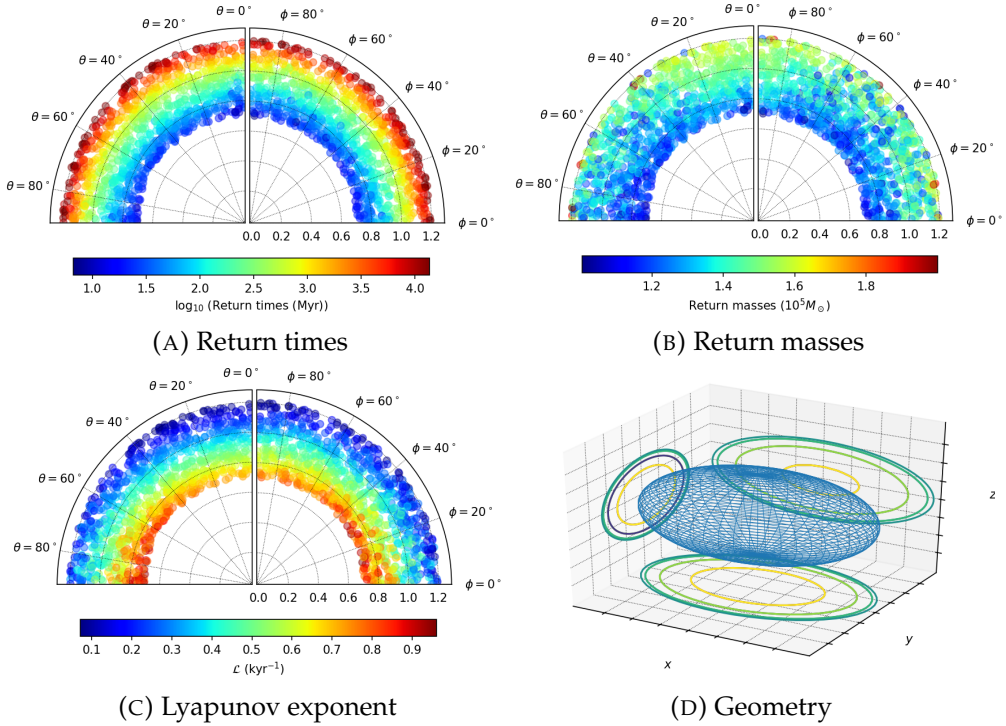


FIGURE D.15: Distribution of the different properties for the galaxy with $a_1 = 1$, $a_2 = 6.4 \times 10^{-1}$, $a_3 = 5.5 \times 10^{-1}$.

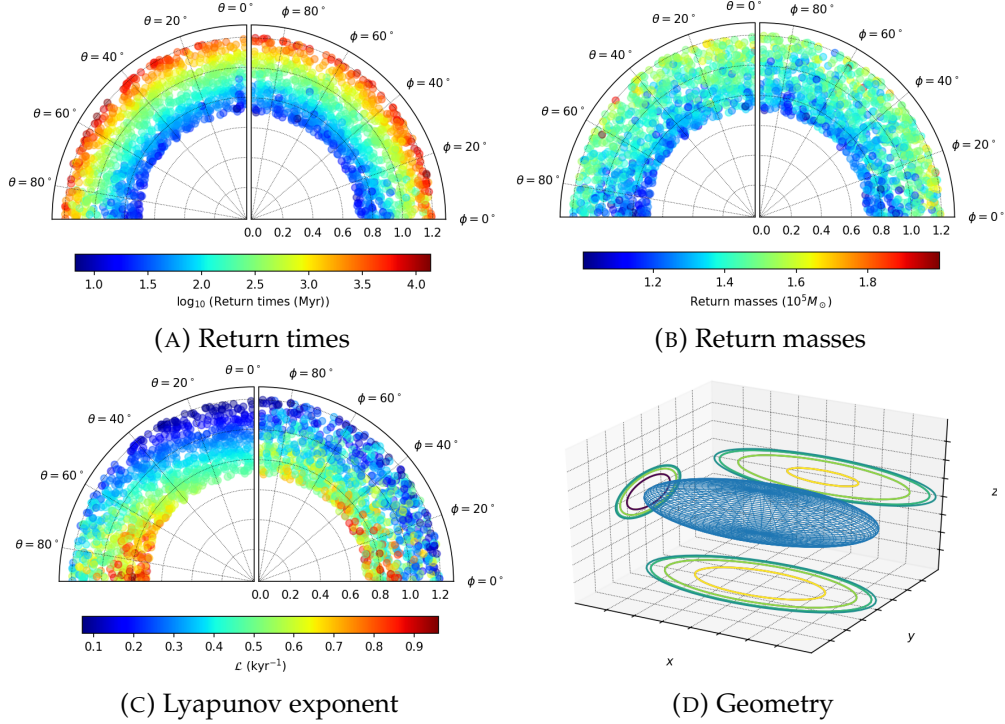


FIGURE D.16: Distribution of the different properties for the galaxy with $a_1 = 1$, $a_2 = 4.8 \times 10^{-1}$, $a_3 = 2.9 \times 10^{-1}$.

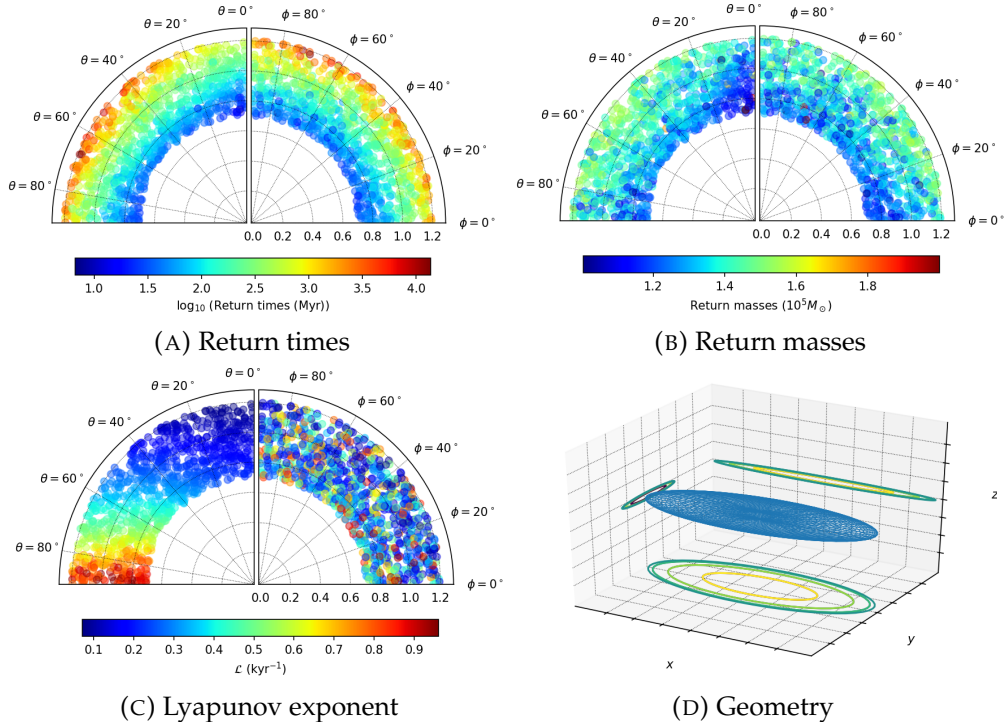


FIGURE D.17: Distribution of the different properties for the galaxy with $a_1 = 1$, $a_2 = 3.9 \times 10^{-1}$, $a_3 = 5.2 \times 10^{-2}$.

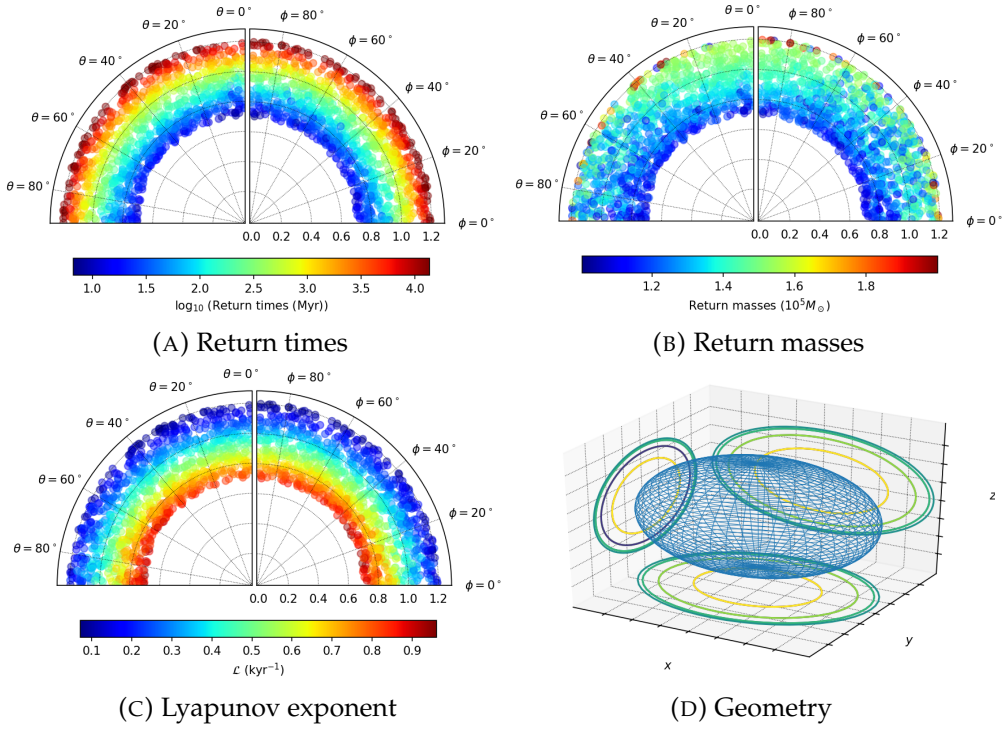


FIGURE D.18: Distribution of the different properties for the galaxy with $a_1 = 1$, $a_2 = 7.5 \times 10^{-1}$, $a_3 = 7.1 \times 10^{-1}$.

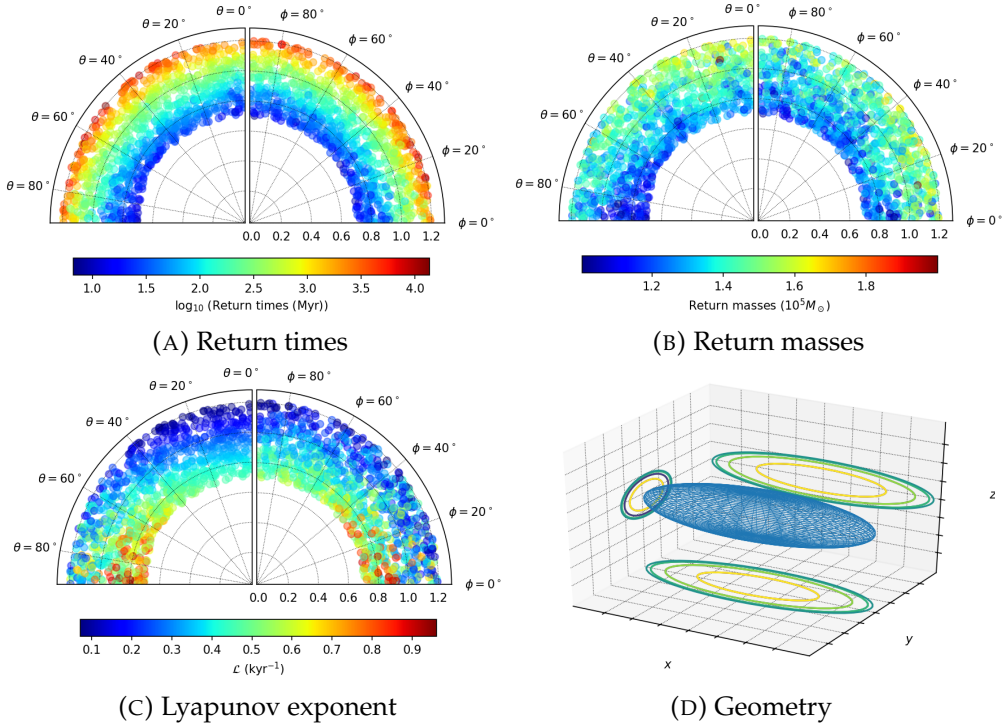


FIGURE D.19: Distribution of the different properties for the galaxy with $a_1 = 1$, $a_2 = 3.7 \times 10^{-1}$, $a_3 = 2.8 \times 10^{-1}$.

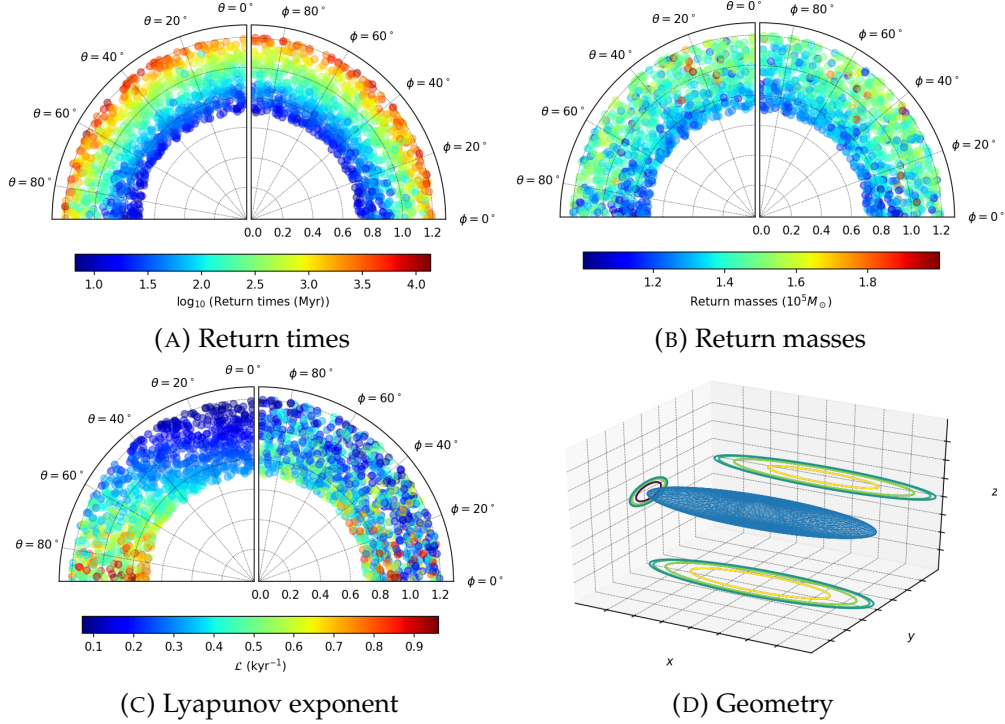


FIGURE D.20: Distribution of the different properties for the galaxy with $a_1 = 1$, $a_2 = 2.8 \times 10^{-1}$, $a_3 = 1.5 \times 10^{-1}$.

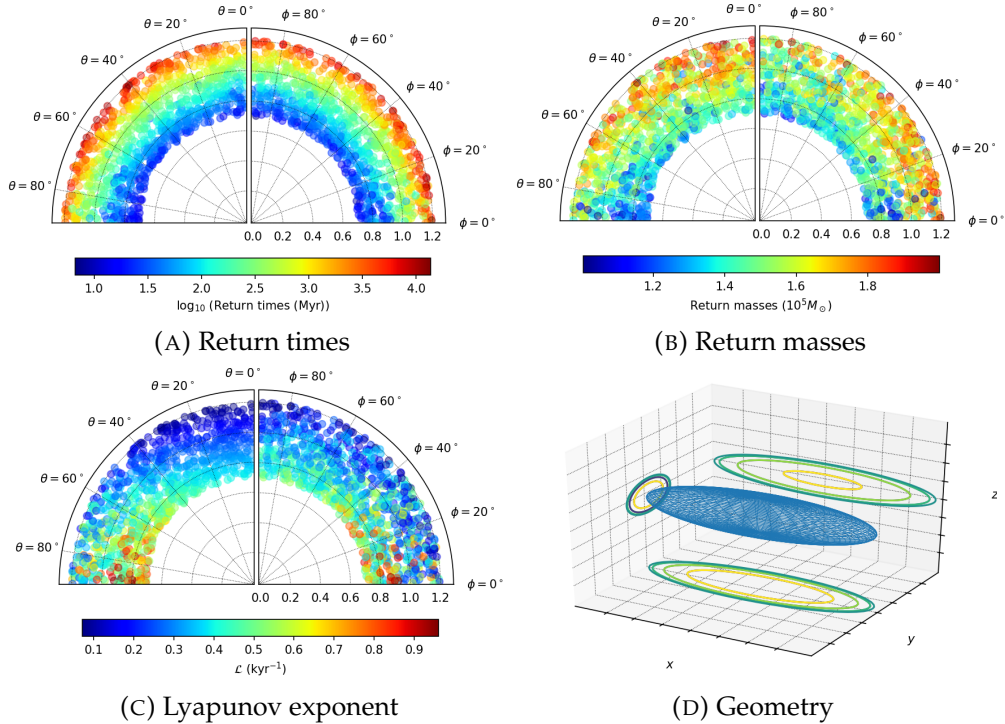


FIGURE D.21: Distribution of the different properties for the galaxy with $a_1 = 1$, $a_2 = 3.2 \times 10^{-1}$, $a_3 = 2.4 \times 10^{-1}$.

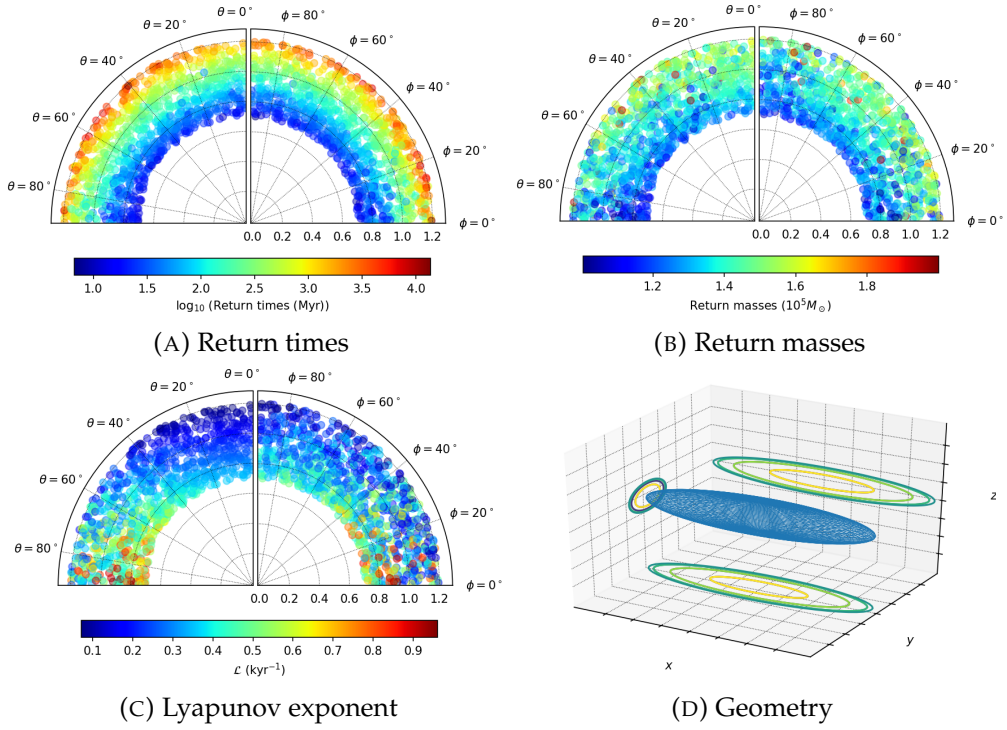


FIGURE D.22: Distribution of the different properties for the galaxy with $a_1 = 1$, $a_2 = 2.7 \times 10^{-1}$, $a_3 = 2.0 \times 10^{-1}$.

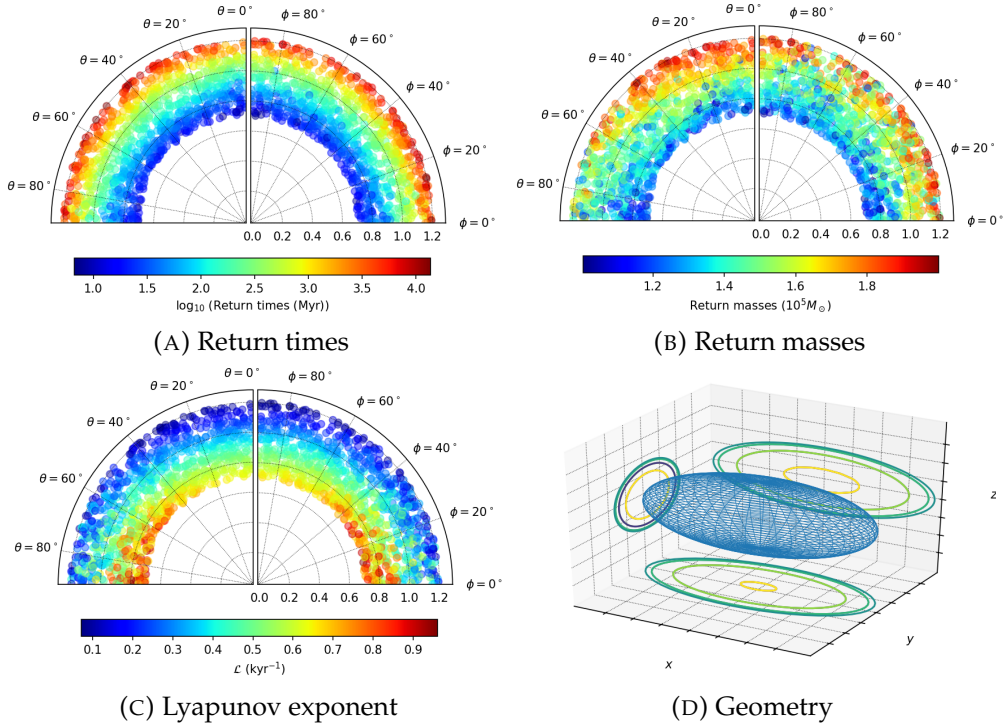


FIGURE D.23: Distribution of the different properties for the galaxy with $a_1 = 1$, $a_2 = 4.8 \times 10^{-1}$, $a_3 = 4.6 \times 10^{-1}$.

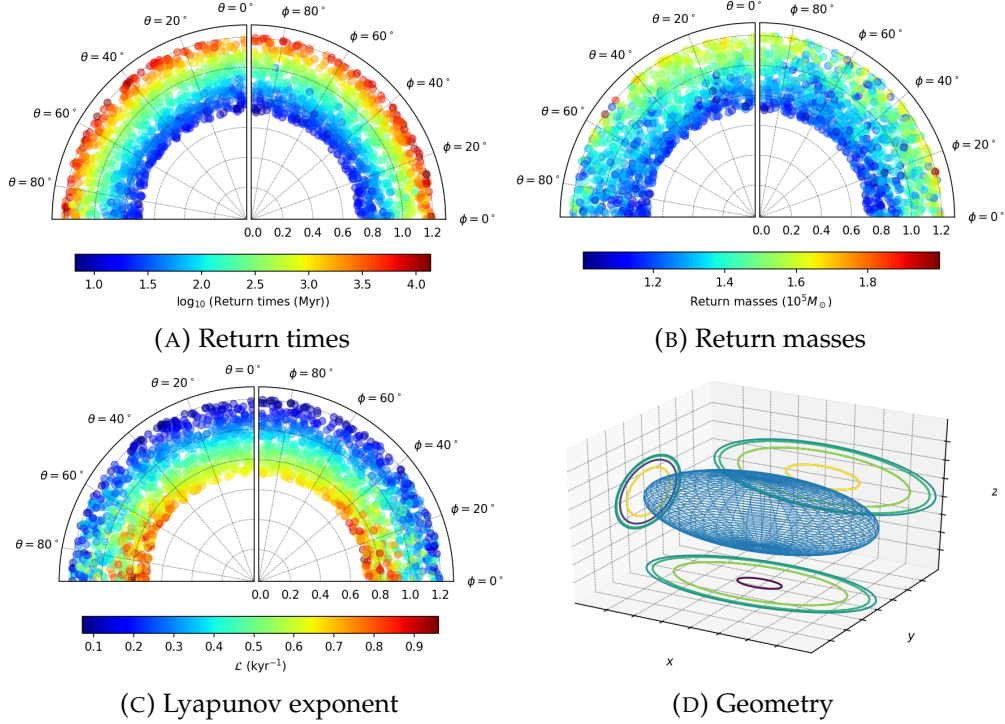


FIGURE D.24: Distribution of the different properties for the galaxy with $a_1 = 1$, $a_2 = 4.8 \times 10^{-1}$, $a_3 = 4.6 \times 10^{-1}$.

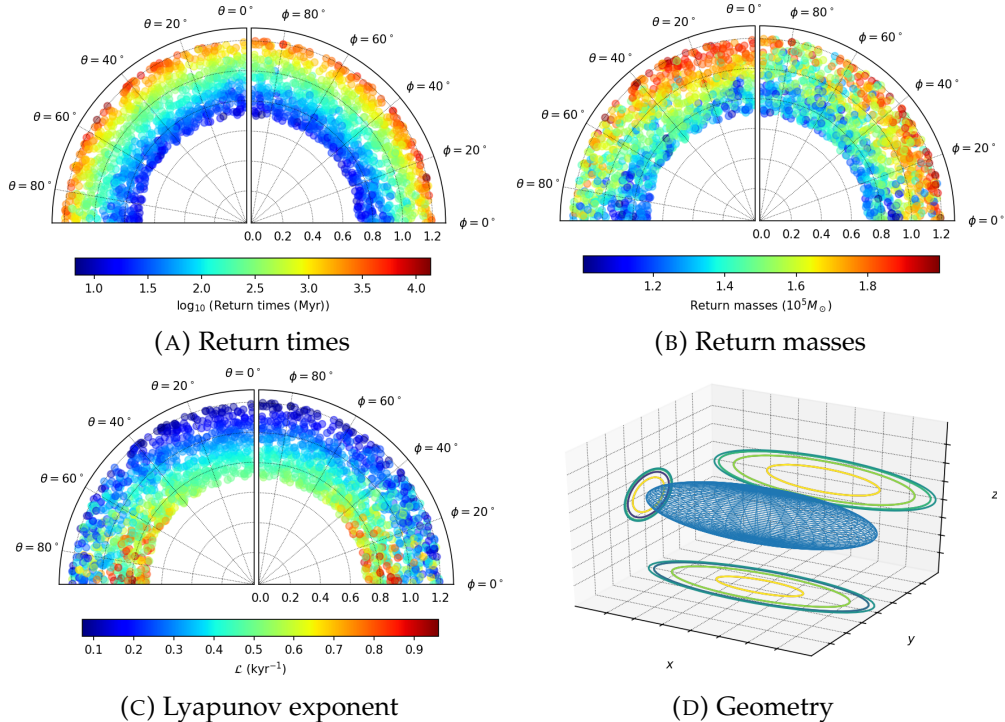


FIGURE D.25: Distribution of the different properties for the galaxy with $a_1 = 1$, $a_2 = 3.5 \times 10^{-1}$, $a_3 = 3.3 \times 10^{-1}$.

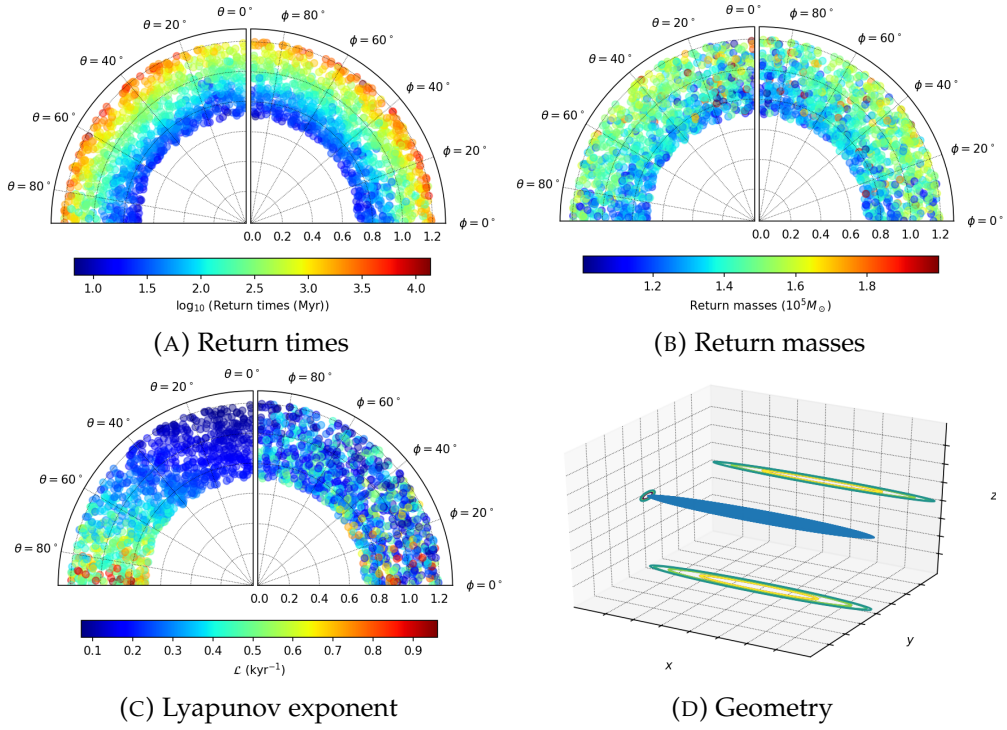


FIGURE D.26: Distribution of the different properties for the galaxy with $a_1 = 1$, $a_2 = 1.1 \times 10^{-1}$, $a_3 = 5.3 \times 10^{-2}$.

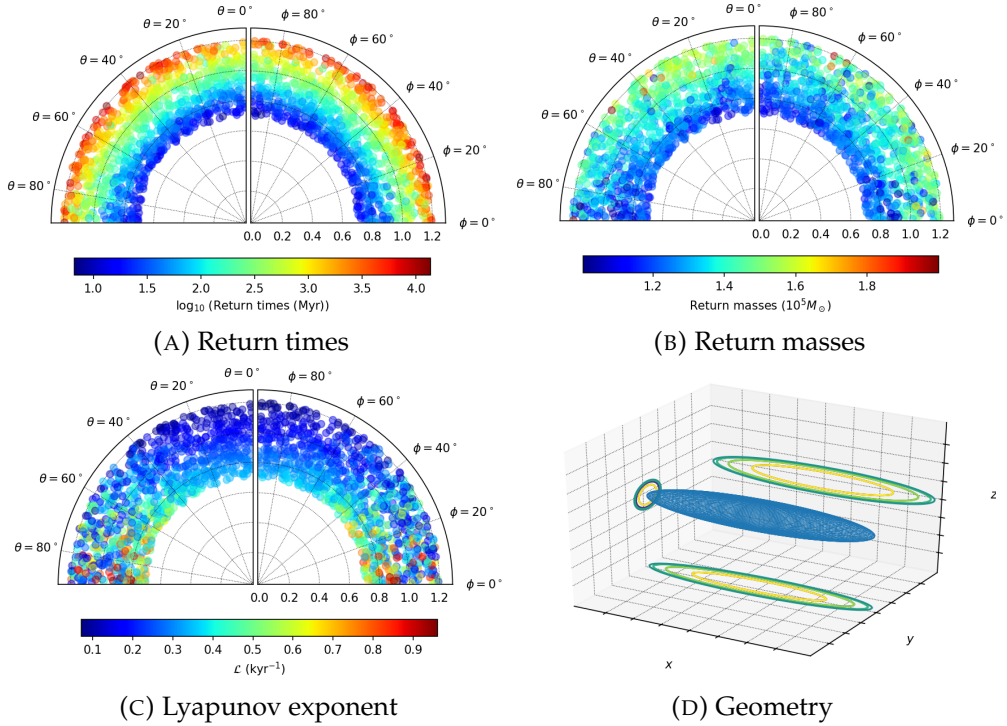


FIGURE D.27: Distribution of the different properties for the galaxy with $a_1 = 1$, $a_2 = 2.0 \times 10^{-1}$, $a_3 = 1.9 \times 10^{-1}$.

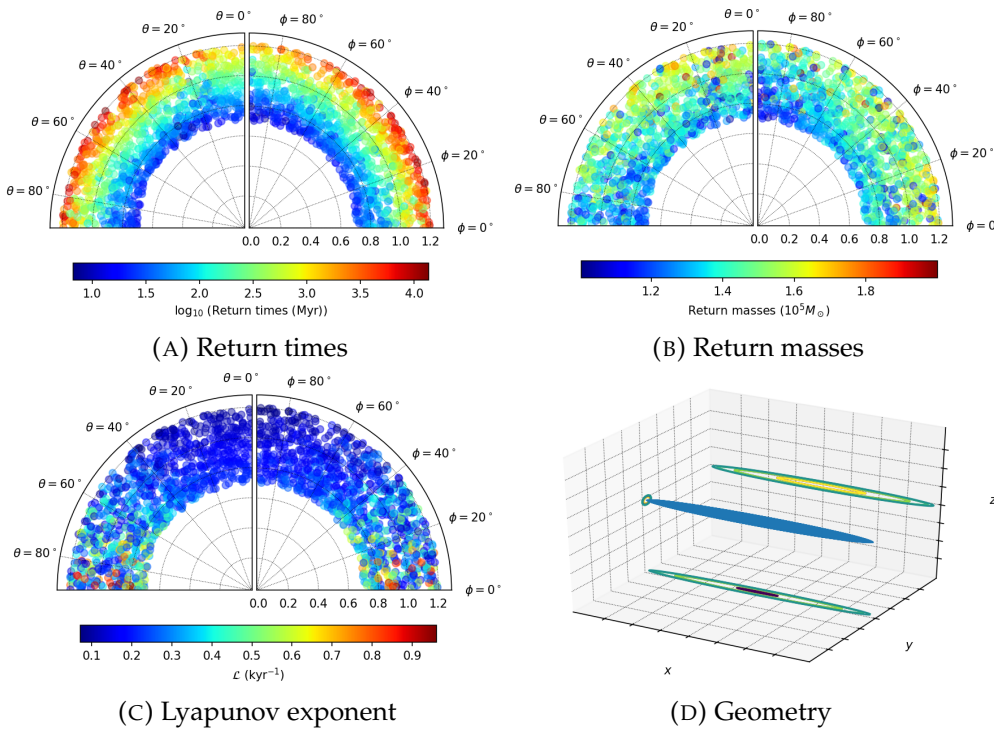


FIGURE D.28: Distribution of the different properties for the galaxy with $a_1 = 1$, $a_2 = 6.6 \times 10^{-2}$, $a_3 = 6.1 \times 10^{-2}$.

References

- (1) Straumann, N., *General relativity*; Springer Science & Business Media: 2012.
- (2) Bassan, M. *Astrophysics and Space Science Library* **2014**, 404, 275–290.
- (3) Hoyng, P. *Relativistic Astrophysics and Cosmology: A Primer* **2006**, 133–154.
- (4) Brügmann, B. *Science* **2018**, 361, 366–371.
- (5) Hughes, S. A.; Favata, M.; Holz, D. E. In *Growing Black Holes: Accretion in a Cosmological Context*; Springer: 2005, pp 333–339.
- (6) Bonnor, W.; Rotenberg, M. *Proc. R. Soc. Lond. A* **1966**, 289, 247–274.
- (7) Choksi, N.; Behroozi, P.; Volonteri, M.; Schneider, R.; Ma, C.-P.; Silk, J.; Moster, B. *Monthly Notices of the Royal Astronomical Society* **2017**, 472, 1526–1537.
- (8) Baker, J. G.; Boggs, W. D.; Centrella, J.; Kelly, B. J.; McWilliams, S. T.; Miller, M. C.; Van Meter, J. R. *The Astrophysical Journal Letters* **2008**, 682, L29.
- (9) Tanaka, T.; Haiman, Z. *The Astrophysical Journal* **2009**, 696, 1798.
- (10) Ostriker, E. C. *The Astrophysical Journal* **1999**, 513, 252.
- (11) Escala, A.; Larson, R. B.; Coppi, P. S.; Mardones, D. *The Astrophysical Journal* **2005**, 630, 152.
- (12) Buote, D. A.; Jeltema, T. E.; Canizares, C. R.; Garmire, G. P. *The Astrophysical Journal* **2002**, 577, 183.
- (13) Binney, J. *Comments on Astrophysics* **1978**, 8, 27–36.
- (14) Larson, J.; Sarid, G. In *Lunar and Planetary Science Conference*, 2017; Vol. 48.
- (15) Binney, J.; Tremaine, S., *Galactic dynamics*; Princeton university press: 2011; Vol. 20.
- (16) Hernquist, L. *The Astrophysical Journal* **1990**, 356, 359–364.
- (17) Madau, P.; Quataert, E. *The Astrophysical Journal Letters* **2004**, 606, L17.
- (18) Barkana, R.; Loeb, A. *Physics reports* **2001**, 349, 125–238.
- (19) Sorai, K.; Nakai, N.; Kuno, N.; Nishiyama, K.; Hasegawa, T. *Publications of the Astronomical Society of Japan* **2000**, 52, 785–802.
- (20) Bañados, E.; Venemans, B. P.; Mazzucchelli, C.; Farina, E. P.; Walter, F.; Wang, F.; Decarli, R.; Stern, D.; Fan, X.; Davies, F. B., et al. *Nature* **2018**, 553, 473.

- (21) Pâris, I.; Petitjean, P.; Aubourg, É.; Myers, A. D.; Streblyanska, A.; Lyke, B. W.; Anderson, S. F.; Armengaud, É.; Bautista, J.; Blanton, M. R., et al. *Astronomy & Astrophysics* **2018**, *613*, A51.
- (22) Aghanim, N; Akrami, Y; Ashdown, M; Aumont, J; Baccigalupi, C; Ballardini, M; Banday, A.; Barreiro, R.; Bartolo, N; Basak, S, et al. *arXiv preprint arXiv:1807.06209* **2018**.
- (23) Poon, M.; Merritt, D *The Astrophysical Journal* **2001**, *549*, 192.
- (24) Morbidelli, A., *Modern celestial mechanics: aspects of solar system dynamics*, 2002.
- (25) Muñoz-Gutiérrez, M.; Reyes-Ruiz, M; Pichardo, B *Monthly Notices of the Royal Astronomical Society* **2015**, *447*, 3775–3784.
- (26) Benettin, G.; Galgani, L.; Giorgilli, A.; Strelcyn, J.-M. *Meccanica* **1980**, *15*, 9–20.